

# Flow coupling between active and passive fluids across interfaces of compressed active droplets

Yen-Chen Chen<sup>1</sup>, Brock Jolicoeur<sup>2</sup>, Chih-Che Chueh<sup>3</sup>, and Kun-Ta Wu<sup>1,2,4,\*</sup>

<sup>1</sup>Department of Mechanical Engineering, Worcester Polytechnic Institute, Worcester, Massachusetts 01609, USA

<sup>2</sup>Department of Physics, Worcester Polytechnic Institute, Worcester, Massachusetts 01609, USA

<sup>3</sup>Department of Aeronautics and Astronautics, National Cheng Kung University, Tainan 701, Taiwan

<sup>4</sup>The Martin Fisher School of Physics, Brandeis University, Waltham, Massachusetts 02454, USA

## Abstract

Interfaces mediate fluid–fluid interactions among different immiscible liquids. Here, we demonstrated that active fluids can induce oil flows across water–oil interfaces and that the oil flows can, in return, alter the self-organization of the active fluid. We created interface by immersing an active fluid in a compressed water-in-oil droplet. The droplet geometry supported the formation of intra-droplet circulatory flows, but the flows turned chaotic when the thickness of the oil layer surrounding the droplet was decreased. We showed that the flow transition was due to active fluid–oil flow coupling across the interface, with a millimeter-scale coupling length. These results were reproduced with a continuum active fluid simulation. Finally, we developed two milli-fluidic devices that could trigger or suppress intra-droplet circulatory flows in real time. One device achieved such control by locally deforming the droplet; the other by decreasing the surrounding oil layer thickness without contacting the droplet.

## Introduction

Active fluids consume local fuels to overcome equilibrium constraints so as to flow spontaneously without external energy input.<sup>1–10</sup> Such spontaneous flows of active fluids have been reported to depend on geometries of system boundaries; in particular, when the boundaries were circular or racetrack-like, the active fluids self-organized into circulatory flows or river-like flows.<sup>11–24</sup> Aside from boundary geometries, boundary conditions were shown to play an influential role in the self-organization of active fluid systems.<sup>25–27</sup> For example, when active fluids were confined in a droplet immersed in liquid crystal, the liquid crystal developed oscillating rings surrounding the droplet,<sup>28–31</sup> demonstrating that the droplet surface created a fluid boundary that allowed active fluid to alter the passive fluid configuration on the opposite side of the boundary. This example illustrates that a fluid boundary can induce a hydrodynamic coupling between active and passive fluids near their interface.<sup>32</sup> However, this fluid boundary-induced coupling, along with its influence on active fluid flows, remains poorly understood.<sup>33</sup> The lack of a complete understanding of this coupling limits the development of active fluid applications that involve interfaces. For example, droplets encapsulating active fluid (i.e., active droplets) were reported to self-propel when compressed between a pair of parallel glasses.<sup>34</sup> This self-propelling feature could be applied to develop microfluidic devices that allow a group of drug-filled active droplets to self-assemble and collectively migrate for drug delivery.<sup>35</sup> To realize this application, understanding how droplets interact is indispensable; investigating droplet–droplet interactions requires knowledge of how flows of active and passive fluids couple across their interfaces. In this study, we systematically characterized the coupling between active and passive fluids near their interfaces. We focused on how active fluids drive passive fluids through interfaces and on how the passive fluid configuration can, in return, influence the self-organization of active fluids, along with the associated characteristic length of this active–passive fluid coupling. To gain deeper insight into our experimental work, we developed a continuum complex fluid simulation based on established active fluid models. The simulations not only predicted the active–passive fluid coupling but also qualitatively agreed with our experimental outcomes, demonstrating the applicability of established active fluid models in experimental active fluid systems. Finally, we demonstrated two methods to direct

active fluid flows by manipulating interfacial dynamics. One method utilized a milli-fluidic device to deform the interfaces *in situ*; the other method altered the passive fluid configuration near the interface without physically contacting the droplet. Both methods provided real-time control on guiding the active fluid to flow coherently or chaotically. This work on active–passive fluid coupling advances our knowledge of the self-organization of confined active fluids and will promote the development of active fluid applications.

## Results

**Kinesin-driven microtubule-based active fluids.** To investigate the active–passive fluid coupling across the interface, we chose microtubule–kinesin complex active fluid as the active component in our experiments because this active fluid has been reported to be tunable and reproducible and the established characterizations and modeling can serve as our references in our study.<sup>36–40</sup> The fluids were driven by extensile microtubule bundles that were assembled by depletion and extended by kinesin motor clusters (Fig. 1a).<sup>41</sup> The bundles repeatedly extended, broke, and annealed, resulting in an active gel network whose structure was constantly rearranged.<sup>34</sup> The rearranging active gel stirred the surrounding liquid (96% water), causing flows. Such flows of active fluid were reported to develop spontaneous circulatory flows when confined in a cylindrical no-slip solid boundary.<sup>11</sup> However, when the boundary condition is changed from no-slip solid to fluid without altering the boundary geometry, it is unknown how the circulatory flows would respond. In this study, we investigated how the circulatory flows of active fluid are influenced by the fluid characteristic of fluid cylindrical boundaries in order to elucidate how active and passive fluids interact near fluid boundaries.

**Confining the active fluid in an immobilized active droplet.** To create a fluid cylindrical boundary, we confined the active fluid in a water-in-oil droplet compressed between a pair of plates. Because of interfacial tension, the droplet was deformed into a cylinder-like geometry.<sup>42</sup> Because the droplet interface was positioned between two types of fluids (oil and water), the interface was fluid.<sup>43</sup> As such, the compressed droplet provided a fluid cylindrical boundary to confine the active fluid. However, the compressed droplet was motile,<sup>33,34,44</sup> so we curved the top plate into a dome-like shape to fix the droplet at the dome center to allow the long-term observation of the intra-droplet flows (Fig. 1b). We observed that the confined flows self-organized into a droplet-wise circulatory flow (Video S1)<sup>13</sup> and that the circulation depended on the thickness of the oil layer surrounding the droplet (Fig. 1c). A thicker oil layer supported the intra-droplet circulatory flows, which were suppressed when the thickness of the oil layer was decreased (Video S2).

To quantify the coherence of the circulatory flows, we added fluorescent tracer particles to track the fluid flows. The circulation order parameter (COP) was defined as the average fraction of the azimuthal component in the flow velocity:  $\text{COP} \equiv \langle v_{i,\theta} / |\mathbf{v}_i| \rangle_i$ , where  $v_{i,\theta}$  is the azimuthal component of velocity  $\mathbf{v}_i$  of the  $i^{\text{th}}$  tracer, and  $\langle \rangle_i$  indicates averaging of the tracer particles.<sup>11</sup>  $\text{COP} = 1$  indicates a perfect counterclockwise circulation;  $\text{COP} = -1$  indicates a perfect clockwise circulation; and  $\text{COP} = 0$  indicates a random flow. The COP analyses revealed that the circulatory flow took approximately 1 hour to develop but remained at a steady state for hours thereafter. By contrast, the COP fluctuated in the shrunken oil (Fig. 1d). These results demonstrated that self-organization of the active fluid confined in fluid boundaries depended on parameters outside the boundaries; thus, there was a need to systematically characterize how the intra-droplet fluid behaviors were influenced by the geometric parameters of oils as well as droplets.

**Formation of intra-droplet circulatory flows depended on the geometries of droplets and oils.** To investigate how the intra-droplet flows were influenced by the shapes of the droplets and oils, we first prepared a series of oil baths ( $R = 5$  mm) that immersed various compressed active droplets with the same height ( $h = 1$  mm) but different radii ( $r = 0.5$ –5 mm), followed by measuring the corresponding circulation

order parameters. Our measurements revealed that circulatory flows developed when the droplet radii were smaller than a critical radius ( $r_c \approx 2.4$  mm); enlarging the droplets above this limit suppressed the circulatory flows (Fig. 2a). Moreover, we found that such critical radius was reduced ( $r_c \approx 1.3$  mm) when the oil bath was shrunken ( $R = 3.5$  mm; Fig. 2b), demonstrating the role of oil configuration in the formation of intra-droplet circulatory flows.

**Circulatory flows within water-in-oil droplets depended on the oil layer thicknesses.** To characterize the influence of the oil configuration on intra-droplet flows, we systematically varied the size of the oil bath ( $R$ ), or equivalently the thickness of the oil layer surrounding the droplet ( $\Delta \approx 0$ –11 mm) while fixing the droplet shape ( $r \approx 2.4$  mm,  $h = 2$  mm), followed by measuring the circulation order parameter as a function of oil layer thickness (Fig. 3a). Our measurements revealed that the intra-droplet flows were sensitive to oil configurations when the oil layers were thinner than a critical thickness ( $\Delta_c \approx 4$  mm); oil layers thicker than this limit did not influence intra-droplet flows. Based on this observation, we hypothesized that such critical thickness of oil layers originated from the water–oil coupling near the interface, which should not be sensitive to droplet geometries.<sup>44</sup> To test our hypothesis, we repeated the measurements on three different droplets (Figs. 3b–d). Our repeated measurements showed that across our explored droplet geometries, there existed a similar critical thickness. When the oil layer was thinner than this thickness, the circulation order parameters varied quickly, whereas when it was thicker, the circulatory flows remained intact. Such a universal critical thickness implied that the intra-droplet active fluid was coupled to the oil within the critical thickness from the interface, which is consistent with our hypothesis.

To investigate how this coupling affected the flow rates of intra-droplet circulation, we analyzed the flow profiles of azimuthal velocities and found out that the oil layer thickness influenced the flow velocity (Figs. 3e–h). Thickening oil layers irregularly accelerated, decelerated, or even ceased circulatory flows, which agreed with our measurements in circulation order parameters (Figs. 3a–d). Such irregularity revealed a nonlinear influence of the water–oil coupling on circulatory flows. Despite the complex nature of the water–oil coupling, our data demonstrated that the oil configuration could direct the self-organization of intra-droplet active fluid through the water–oil interface.

**The oil layer thickness influenced intra-droplet microtubule-based network structure.** The intra-droplet fluid flows were powered by a kinesin-driven, microtubule-based network. To explore whether this network structure was affected by the oil configuration, we imaged the network with confocal microscopy and analyzed the images with the snake algorithm to extract the network structure and reveal the bundle orientational distributions (Figs. 4b&c).<sup>45</sup> Our analyses revealed that when the droplet ( $r \approx 2.4$  mm,  $h = 1$  mm) developed circulatory flows, the microtubule bundles mostly aligned near the water–oil interface (blue solid curve in Fig. 4c). The alignment faded with increasing distance from the interface until reaching the droplet center where the microtubule bundles oriented randomly (red and green solid curves). These observations demonstrated that circulatory flows within droplets were accompanied with a thin nematic layer of microtubule bundles near water–oil interface.<sup>11</sup> Furthermore, such formation of the nematic layer was suppressed when the thickness of the oil layer was decreased (dashed curves), implying that fluid dynamics in oils could penetrate water–oil interfaces to influence the self-rearrangement of the microtubule-based network in the droplet, consistent with our observations on the oil layer-dependent circulatory flows (Fig. 3).

**Active fluid induced chaotic flows in oil.** Our data demonstrated that the layer thickness of the oil used to immerse the droplet influenced the self-organization of the intra-droplet active fluid flows. This finding suggested an interaction between flows in the oil and in the droplet. To reveal such a water–oil interaction, we monitored the flows both in oil ( $\Delta \approx 2.4$  mm) and in the droplet ( $r \approx 2.4$  mm,  $h = 1$  mm). To distinguish the flows in both regimes, we doped the oil with 1- $\mu$ m tracers and the droplet with 3- $\mu$ m tracers (Fig. 5a).

We monitored the tracers for 1 hour, tracked the tracer motion to analyze the flows in the oil and droplet, and plotted the time-averaged velocity field and vorticity map (Fig. 5b). Our analysis showed that the intra-droplet active fluid developed a circulatory flow, as expected from our data (Fig. 3b), but there was no observable net flow in oil. To confirm the lack of net oil flows, we analyzed the flow profiles of azimuthal velocities, which showed that the active fluid developed  $\sim 6 \mu\text{m/s}$  circulatory flows within the droplet, but the flow vanished when crossing the water–oil interface (blue curve in Fig. 5c). When the thickness of the oil layer was decreased ( $\Delta \approx 1.1 \text{ mm}$ ), the circulatory flows were suppressed, but the net oil flows remained absent. However, the absence of net oil flows did not necessarily imply a quiescent oil, as zero net flows could also result from chaotic flows whose velocities canceled out over a time average.<sup>11</sup> To investigate the flow activity in the oil and in the droplet, we analyzed flow speed profiles, which showed that oil near the interface developed 2–4  $\mu\text{m/s}$  chaotic flows that decayed with distance into the oil regime, with a decay length of  $\sim 0.5 \text{ mm}$  (Fig. 5d). This decay length suggested that the dynamics of the intra-droplet active fluid were coupled to the oil near the interface with a millimeter-scale coupling length, which implies that disturbances to the oil (such as stirring) within this coupling range might influence the intra-droplet active fluid flows even if the disturbance does not physically contact the droplet. Conversely, when the disturbance is outside this coupling range, the active fluid might remain intact. This suggestion was consistent with our observation that the arrangement of the oil immersing a droplet affected the formation and deformation of the intra-droplet circulatory flows when the oil layer was thinner than a critical thickness (Fig. 3).

Our result on oil flow characterization is qualitatively consistent with the model prediction by Young *et al.* who predicted that the oil remained quiescent when the active droplet developed circulation and was driven to flow otherwise.<sup>46</sup> Our data showed that the oil flow only developed near the water–oil interface when the droplet was in a circulating state (blue curve in Fig. 5d) but extended to the container surface ( $\rho = 1.1 \text{ mm}$ ) when the droplet was in a chaotic state (red curve). However, Young *et al.* predicted that the intra-droplet circulation was accompanied with a counter-rotation near the water–oil interface, which was observed in bacterial-based active droplet,<sup>14</sup> whereas our data did not show this counter-rotation (Figs. 3e-h and 5c). We argue that the reason accounting for this discrepancy was system dimensionality as Young *et al.*'s model and the bacterial-based active droplet system were both two-dimensional, whereas our active droplet was a three-dimensional system where the ceiling and floor of confinement might have induced additional friction that inhibited the development of counter-rotation near the interface.

**Continuum active fluid simulation qualitatively agreed with experimental outcomes.** We demonstrated that the coupling of flows within and outside droplets influenced the self-organization of intra-droplet flows. Simultaneously, the active fluid was modeled using swimmer-based simulation, where active fluid flows result from the collective motion of interacting active particles,<sup>47,48</sup> and continuum equations of mean fields of active particles (either polar<sup>49-52</sup> or nematic<sup>53-55</sup>), which treat active particle-induced active stress as the driving force that leads to field instability and induces self-driven flows.<sup>56</sup> The model was also applied to describe the active fluid encapsulated in a water-in-oil droplet, and it has been reported that intra-droplet flows can induce flows in oil.<sup>33</sup> However in the model, whether the configuration of oil (such as the oil layer thickness) can, in return, influence self-organization of intra-droplet flows remains untested. To test capability of the model to describe an oil-induced influence and to investigate the fluid mechanics in our active droplet-based experimental system, we adopted the active fluid model established by Gao *et al.* because their model not only includes multiphase fluids (oil and water) along with associated interfaces, but it also succeeds in describing the self-propelling and self-rotating characteristics of active droplets.<sup>33</sup> To adopt the model to our experimental system, we first expanded the model from 2D to 3D, which matched our system dimension but increased the computation load. To increase the computation efficiency, we artificially fixed water–oil interfaces, which matched to our experimental arrangement of immobilizing active droplets using curved ceilings (Fig. 1b). The model contained four main ingredients: (1)

Conservation of mass (the Smoluchowski equation),<sup>57</sup> (2) Fluid mechanics (the Navier–Stokes equation), (3) Interfacial tension force,<sup>58</sup> and (4) Nematic order-induced active stress.<sup>59</sup> To numerically solve these equations to determine the evolution of solvent flows, we adopted the finite element method and evolved the equations for 3 hours of model time.<sup>60,61</sup> To test the model’s capability to describe our experimental system, we arranged two simulation systems with identical droplets ( $r = 2.4$  mm,  $h = 2$  mm) that were immersed in oil layers of different thicknesses ( $\Delta = 1.1$  and 2.6 mm). The simulation revealed that the droplet immersed in the thicker oil layer developed stable persistent intra-droplet circulatory flows. By contrast, in the thinner oil layer, the circulatory flows were suppressed, and the flows remained chaotic (Figs. 6a&b inset), suggesting that in the simulation, the thickness of the oil layer influenced the intra-droplet flows. To characterize the oil-induced influence, we systematically varied the oil layer thickness (0–9.6 mm) while maintaining the droplet geometry, and then analyzed the time-averaged circulation order parameter within each droplet (Fig. 6b). Our analysis showed that the circulation order parameter was sensitive to the oil layer thickness when the layer was thinner than  $\sim 2.2$  mm, suggesting that the flows within and outside droplets were coupled. To reveal such coupling, we analyzed the flow profiles of azimuthal velocities across water–oil interface (Fig. 6c), which showed that intra-droplet circulatory flows induced a thin layer of circulatory flow in oils with a layer thickness of 0.3–2 mm. For the non-circulating droplet, the intra-droplet flows were chaotic and did not induce net flows in oil. However, our analysis on the flow speed profiles revealed that oil near the interface developed flows with a thickness of  $\sim 1$  mm (magenta curve in Fig. 6c inset), suggesting that intra-droplet fluid flows of active fluid induces oil flows near the interface (a more rigorous analysis on active fluid–oil coupling from a perspective of cross-correlation function is available in the Supplementary Information and Fig. S4). These simulation outcomes were qualitatively consistent with our experimental characterizations of the coupling of intra-droplet and extra-droplet flows (Figs. 3&5). These consistencies demonstrated that the simulation model could describe the oil–water coupling, as well as how the coupling influenced the intra-droplet flows of active fluid. However, the simulation failed to match two of our experimental outcomes. First, the simulation showed that the intra-droplet fluid flows became chaotic when oil layers were thicker than  $\sim 5.6$  mm (Fig. 6b), whereas in our experimental data, the intra-droplet fluid flows were insensitive to the oil arrangement when the oil layers were thicker than  $\sim 4$  mm. Second, the simulation predicted the induction of circulatory flows in oil driven by intra-droplet circulation (Fig. 6c), whereas in the experiments, oil developed no net flows regardless of how the fluid flowed within droplets (Fig. 5c). We argued that these discrepancies could be mitigated by removing the constraints on fixing the water–oil interface and allowing the interface to deform, following the rules of spontaneous phase separation of oil and water (the Cahn–Hilliard model),<sup>62</sup> which was neglected in our simulation to achieve a more efficient computation. Overall, despite these discrepancies, our simulation model qualitatively agreed with the experimental outcomes and thus opened the door to utilizing the established simulation platform to guide experimental design in active droplet systems.

**Triggering and suppressing intra-droplet circulatory flows in real time.** We demonstrated that the formation of intra-droplet circulatory flows depends on droplet geometries and the oil layer thickness (Figs. 2&3). This knowledge suggested the feasibility of designing milli-fluidic devices that can manually shape droplets or tune the oil layer thickness to control the formation and deformation of circulatory flows in real time. To manually tune the oil layer thicknesses, we compressed an active droplet ( $h = 2$  mm,  $r \approx 2.4$  mm) in a cylindrical container whose wall was movable (pink blades in Fig. 7a). Moving the wall toward the droplet reduced the amount of oil surrounding the droplet (minimum oil layer thickness  $\Delta_m \approx 1.2$  mm; Fig. 7a left). This arrangement resulted in chaotic flows of active fluid ( $|\text{COP}| \lesssim 0.2$ ; Fig. 7b). To trigger circulatory flows, we moved the wall away from the droplet to increase the oil layer thickness ( $\Delta_m \approx 2.6$  mm; Fig. 7a middle); after  $\sim 30$  minutes, the active fluid developed circulatory flows ( $\text{COP} = 0.4\text{--}0.6$ ; Fig.

7b). The flows lasted for  $\sim 1$  hour and then transitioned to chaotic flows after we moved the wall back toward the droplet ( $\Delta_m \approx 1.2$  mm; Fig. 7a right). These results demonstrated that we could develop and inhibit intra-droplet circulatory flows locally (Video S3), which implied the feasibility of controlling intra-droplet active fluid flows in real time without physically contacting the droplet.

To manually shape the droplets, we compressed the droplet in a cylindrical container with a movable ceiling (Fig. 8a). Since the droplet was deformable, tuning the amount of compression on the droplet altered its shape. We first compressed the droplet to a cylinder-like geometry ( $r \approx 2.0$  mm,  $h = 2$  mm), which supported the formation of circulatory flows ( $\text{COP} = 0.4\text{--}0.6$ , Fig. 8b). The circulatory flow persisted for  $\sim 40$  minutes before manually suppressed ( $|\text{COP}| \lesssim 0.2$ ) by lifting the ceiling ( $h = 3$  mm), which shaped the droplet into a taller, cylinder-like geometry ( $r \approx 1.7$  mm,  $h = 3$  mm). Conversely, the intra-droplet circulatory flow could be manually triggered by deforming the droplet from a taller ( $r \approx 1.7$  mm,  $h = 3$  mm) to a shorter ( $r \approx 2.0$  mm,  $h = 2$  mm) cylinder-like geometry, which caused the intra-droplet fluid to first flow irregularly and then to develop a circulatory flow (Fig. 8c). These results demonstrated that manually shaping the droplet could turn on and off intra-droplet circulatory flows locally (Video S4). These findings pave the way for designing fluidic devices that can shape deformable boundaries to direct the self-organization of confined active fluids in real time.

## Discussion

We have demonstrated how the self-organization of a confined active fluid was influenced by fluid boundaries. The influence originated from the coupling of fluids on both sides of a boundary with a millimeter-scale coupling length. Our experimental data indicated that within this coupling range, disturbance outside the boundary influences the formation and deformation of circulatory flows inside the boundary without the need for physically deforming the boundary, in contrast to our previous work where circulatory flows depended solely on the geometry of no-slip solid boundaries.<sup>11</sup> Despite the observation of multi-fluid coupling, the underlying principles governing such coupling, along with associated fluid mechanics, has remained unclear. Thus, understanding such coupling dynamics and their interactions with the boundaries is an essential next step to unravel the dynamic role of fluid boundaries locating at interfaces between passive and active fluids.<sup>63</sup> To investigate this issue, we developed a continuum simulation platform based on existing active fluid models that qualitatively reproduced our experimental outcomes. The simulation platform allows for sweeping multiple parameters to guide experimental designs that efficiently characterize such interfacial coupling.

Our experimental data demonstrated that the formation of intra-droplet circulatory flows depended on the droplet shape and the layer thicknesses of the oil that immersed the droplets. These observations enabled us to develop two milli-fluidic devices that could trigger or suppress intra-droplet circulatory flows in real time. One device allowed for manually compressing droplets to desired shapes that supported or opposed formation of intra-droplet circulatory flows. The other device enabled us to suppress intra-droplet circulatory flows by locally manipulating the oil flows to disturb active fluid flows through the water–oil coupling near the interface without physically contacting the droplets. These two systems provide the biology community with *in vitro* model systems to probe how the deformation of cell membranes or the disturbance of fluids around cells influences intracellular activities. They can also be used in the development of cell treatment modalities for cells that are sensitive to biomedical approaches and can only be treated with physical methods, such as deforming cells and imposing shear flows.<sup>64,65</sup> In mechanical engineering, these systems pave the way to designing an active fluid-driven machine with adjustable output power.<sup>66</sup>

## Methods

**Fabricate milli-fluidic devices.** To confine the active fluid in a cylinder-like water-in-oil droplet, we needed a milli-fluidic device to compress the droplet between a pair of plates separated by  $h = 1\text{--}2$  mm. However, the compressed droplet was self-propelling<sup>33,34,44</sup>. To immobilize the droplet, we also needed to curve the plate surface into a half-oblate spheroidal dome with a thin cylindrical well (height: 0.2 mm; radius: 1 mm) at the dome center (Fig. S1a). The curved surface and thin well were able to immobilize the droplet without significantly impacting the intra-droplet active fluid behaviors (Supplemental information). Finally, to load the oil and active fluid into the milli-fluidic device, we drilled a 3.6 mm-long loading channel with a width 2 mm and height 1.7 mm, and adjoined the channel to a 2.4 mm-long neck that had the same width (2 mm) but shorter height (1.4 mm). To fabricate this chip, we sketched the 3D design (SOLIDWORKS), followed by programming the corresponding tool paths (Esprit). According to these tool paths, we end-milled a  $610 \times 38 \times 6.4$  mm<sup>3</sup> acrylic rectangular bar with a computer numerical control (CNC; McMaster 1227T222). After the milling, the chip was cleaned with sequential 10-min sonications in detergent (Sigma-Aldrich Z805939), ethanol, and 100 mM potassium hydroxide solution sequentially. To complete the fabrication of the milli-fluidic device, the chip was glued to a fluorophilically-treated glass slide (VWR GWBJ17) with epoxy (Bob Smith Industries BSI-201).<sup>67</sup> After the epoxy was cured ( $\sim 10$  min), the milli-fluidic device was ready for loading a water-in-oil active droplet.

**Confine active fluids in a compressed water-in-oil droplet.** To prepare the water-in-oil droplet that encapsulated the active fluid, we prepared the microtubule-based active fluid based on our previous protocols,<sup>34,68</sup> and pipetted the active fluid through the loading channel into the chamber of the fabricated milli-fluidic device that was filled with an oil (hydrofluoroether, 3M Novec 7500) (Fig. S1a). Since the oil would be in contact with the protein-based active fluid, we doped the oil with 1.8% surfactant (perfluoropolyether–polyethylene glycol–perfluoropolyether, RAN Biotechnologies 008-FluoroSurfactant)<sup>67</sup> to stabilize the protein near the water–oil interface. After pipetting, the active fluid formed a water-in-oil droplet that was compressed between the ceiling and floor of the chamber. The compression deformed the droplet into a cylinder-like geometry<sup>42</sup> whose height ( $h$ ) depended on the ceiling–floor separation of the chamber and whose radius ( $r$ ) depended on the pipetted fluid volume. After injecting the active droplet, we sealed the channel with epoxy. However, after the sealing, the sample can form air bubbles that would affect the experimental outcomes. To keep the bubbles away from the droplet, we tilted the sample to direct the air bubbles to exit the chamber into the loading channel through the neck. The neck had a smaller opening that prevented the bubbles from reentering the chamber, leaving the chamber bubble-free (Fig. S1a close-up). The above processes allowed us to prepare a compressed water-in-oil active droplet with the desired dimensions (height  $h$  and radius  $r$ ).

In our experiments, we first varied the droplet radii in a couple of milli-fluidic devices that contained chambers of radii  $R = 3.5$  and 5 mm (Fig. 2). Each of the devices had a half-spheroidal dome with a vertical semi-axis of  $R_a = 0.25$  mm and a horizontal semi-axis matching the chamber radius,  $R_b = R$ . This setup allowed for probing the role of the droplet radii in the formation of the intra-droplet circulatory flows. We also immersed the droplets in oil layers of various thicknesses (Fig. 3). The oil was contained in the chamber whose radius was the sum of the droplet radius and oil layer thickness  $R = r + \Delta$  (Fig. 1b). To avoid the influence of the ceiling shape on the experimental outcomes, we chose a fixed half-spheroidal ceiling ( $R_a = 0.5$  mm,  $R_b = 5$  mm) to cover the chamber. When the chamber was smaller than the ceiling ( $2R < 2R_b$ ), the ceiling was trimmed to fit into the chamber; conversely, when the chamber was larger than the ceiling ( $2R > 2R_b$ ), the ceiling was extended horizontally to match the chamber size (Fig. S1b&c). This arrangement allowed us to investigate how the intra-droplet self-organization of the active fluid was affected only by the chamber size, or the oil layer thickness.

**Image and analyze flows.** To observe the flows of the active fluids and oil, we doped the active fluids with 0.0004% Alexa 488-labeled 3- $\mu\text{m}$  tracer particles (Polysciences 18861-1), which could be imaged with a green fluorescent protein filter cube (excitation: 440–466 nm, emission: 525–550 nm, Semrock 96372). To characterize the flow behaviors, we imaged the tracer sequentially for 3 hours, followed by tracking their trajectories  $\mathbf{x}_i(t)$  with the Lagrangian algorithm.<sup>69</sup> These trajectories revealed the evolution of their velocities  $\mathbf{v}_i(t) \equiv d\mathbf{x}_i(t)/dt$ , which allowed for measuring their circulation order parameter  $\text{COP}(t) \equiv \langle v_{i,\theta}(t)/|\mathbf{v}_i(t)| \rangle_i$ , where  $v_{i,\theta}$  is the azimuthal component of velocity  $\mathbf{v}_i$  of the  $i^{\text{th}}$  tracer, and  $\langle \rangle_i$  indicates averaging of the tracer particles (Fig. 1d). To quantify the coherence of the intra-droplet circulatory flows, we measured the time-averaged circulation order parameter:  $\langle \text{COP}(t) \rangle_t$  (Figs. 2&3a-d). To reveal flow rates of intra-droplet circulatory flows, we measured the flow profiles of the azimuthal velocities across the droplet  $\langle v_\theta(d) \rangle \equiv \langle v_{i,\theta}(d, t) \rangle_{t,i}$ , where  $d$  is the distance from the water–oil interface (Figs. 3e-h).

To reveal the structure of the flows in the droplet, we measured the time-averaged, normalized velocity fields  $\mathbf{V}(\mathbf{x}) \equiv \langle \frac{\mathbf{v}(\mathbf{x}, t)}{|\mathbf{v}(\mathbf{x}, t)|} \rangle_t$  and vorticity distributions  $\Omega(\mathbf{x}) \equiv \langle \frac{\omega(\mathbf{x}, t)}{3\sigma(t)} \rangle_t$ , where  $\mathbf{v}(\mathbf{x}, t)$  is the velocity field measured by analyzing the sequential tracer images with the particle image velocimetry algorithm,<sup>70</sup>  $\omega(\mathbf{x}, t) \equiv [\nabla \times \mathbf{v}(\mathbf{x}, t)]_z$  is the corresponding vorticity distribution, and  $\sigma(t) \equiv \text{std}[\omega(\mathbf{x}, t)]$  is the standard deviation of the vorticity (Fig. 1c).<sup>11</sup> By utilizing the particle tracking and particle image velocimetry algorithms, we quantified the coherences, rates, and structures of the intra-droplet active fluid flows to evaluate how the self-organization of the active fluid responded to changes in the geometric parameters of the droplet and oil.

To characterize flows in oil, we doped the oil with 0.002% Alexa 488-labeled 1- $\mu\text{m}$  tracer particles (Polysciences 18860-1) and conducted the same observations and analyses for active fluid flows (Figs. 5b&c). To reveal flow activities near water–oil interfaces, we measured the flow speed profiles  $\langle |\mathbf{v}(\rho)| \rangle \equiv \langle |\mathbf{v}_i(\rho, t)| \rangle_{t,i}$ , where  $\rho$  is the radial coordinate relative to the water–oil interface (Fig. 5c inset), which demonstrate how fast fluids flow on two sides of an interface (Fig. 5d).

**Image and analyze microtubule-based network structure.** To characterize the influence of the oil layer thicknesses on the intra-droplet microtubule-based network structure, we imaged the microtubules at the droplet midplane using confocal microscopy (Leica SP5 point scanning confocal microscope). The microtubules were labeled with Alexa 647 (following our previous protocol<sup>68</sup>), which were excited with a 633 nm helium-neon laser and observed in a 633–647 nm window. To reveal the microtubule arrangement in a circulating active fluid, we selected the droplet geometry ( $r \approx 2.4$  mm,  $h = 1$  mm) and oil layer thickness ( $\Delta \approx 2.4$  mm) that supported formation of intra-droplet flows based on our data (Fig. 3b). To observe the time-averaged network structure, we imaged the network every 2 seconds for 1 hour and then analyzed the image with the snake algorithm to extract the network structure, which consisted of unit-length segments (Fig. 4b).<sup>45</sup> We stacked the segment orientations from each image and then counted these orientations to reveal the orientational distribution of the microtubule bundles (Fig. 4c). To characterize how the bundles oriented at different locations within the droplet, the distribution was measured near the water–oil interface,  $\sim 400$   $\mu\text{m}$  from the interface, and at the droplet center (blue, red, and green squares in Fig. 4a). To study how the orientational distributions were affected by the oil layer thicknesses, the measurements were repeated on another sample with the same droplet shape but different oil layer thickness ( $\Delta \approx 1.1$  mm) that suppressed intra-droplet circulatory flows based on our data (Fig. 3b). These measurements characterized how the microtubule bundles oriented at various locations within the same shape of droplets immersed in different oil layers (Fig. 4c).

**Establish a continuum simulation platform modeling 3D active droplet systems.** To examine whether existing active fluid models<sup>47-56</sup> could describe our water–oil coupling and to gain deeper insight into the



fluid mechanics of our active droplet systems, we adopted the active droplet model developed by Gao *et al.* because it models the coupling between flows within and outside droplets and has previously suggested the feasibility of developing a self-rotating droplet.<sup>33</sup> To test whether such a model could describe the role of the oil layer thickness in intra-droplet active fluid flows, we first expanded the model from 2D to 3D because our droplet system was three-dimensional. In the three-dimensional droplet system, the model considered two main forces: (1) Interfacial tension force from the droplet surface  $\mathbf{T} \equiv (\gamma K/\epsilon)\nabla c$ , where  $\gamma$  is the water–oil interfacial tension,  $\epsilon$  is the interface thickness,  $K \equiv c(c-1)(c-1/2) - \epsilon^2 \nabla^2 c$  is the chemical potential that characterizes the phase variation within the interface region, and  $c$  is a phase function with  $c = 1$  representing water and  $c = 0$  representing oil,<sup>58</sup> and (2) active stress exerted by extensile microtubule-based bundles in active fluid that was proportional to the orientational order of bundles  $\sigma_a \equiv \alpha c \mathbf{D}$ ,<sup>59</sup> where  $\alpha$  is an activity coefficient,  $\mathbf{D} \equiv \int_p \mathbf{p} \mathbf{p} \psi d\mathbf{p}$  represents the local nematic order of bundles,<sup>71</sup>  $\mathbf{p}$  represents the bundle orientation, and  $\psi$  represents the probability distribution of bundles that satisfies the Smoluchowski equation.<sup>49</sup> These two forces were exerted on incompressible fluids ( $\nabla \cdot \mathbf{u} = 0$ ) to create flows  $\mathbf{u}$  that satisfied the Navier–Stokes equation:

$$\rho \left( \frac{\partial \mathbf{u}}{\partial t} + \mathbf{u} \cdot \nabla \mathbf{u} \right) = \nabla \cdot [-p\mathbf{I} + \mu(\nabla \mathbf{u} + \nabla \mathbf{u}^T)] + \mathbf{F}, \quad (1)$$

where  $\mathbf{F} \equiv \mathbf{T} + \nabla \cdot \sigma_a$  is the net body forces from interfacial tension and extensile bundles,  $\rho$  is the fluid density,  $p$  is the fluid pressure, and  $\mu$  is the dynamic viscosity of fluids. The fluids were confined in no-slip boundaries whose geometries were identical to experimental containers that consisted of a circular side wall, a flat floor, and a curved ceiling (Fig. 1b). The boundary was filled with oil that immersed a compressed active droplet.

To solve the equations so as to determine the evolution of fluid flows  $\mathbf{u}$ , we initialized the flow field with quiescent fluids ( $\mathbf{u} = 0$ ) under uniform pressure ( $p = 0$ ) and evolved the fluid flows for 3 hours of model time using the finite element method based on the computational fluid dynamics software COMSOL Multiphysics<sup>TM</sup>.<sup>60,61</sup> The resulting flow fields allowed for determining the corresponding circulation order parameter and flow profiles (Fig. 6), which were compared with our experimental outcomes (Figs. 3&5). Details of the model are available in Supplementary Information.

**Design wall-movable fluidic devices.** To control the layer thickness of the oil that immersed the droplet in real time, we designed a fluidic device whose wall was movable. The wall-movable device was designed based on the mechanics of a mechanical iris, which has been conventionally used to tune the aperture size of optical devices.<sup>72</sup> However, a conventional mechanical iris component consists of at least six blades. Fabricating a six-blade mechanical iris at the micron scale was challenging because blades at this scale bent spontaneously in our fabrication process and could not be assembled. As such, we simplified the device design to contain only one blade, which allowed the blade to be thick enough (1,000  $\mu\text{m}$ ) to remain flat (pink components in Fig. S6). The thickened blade was pinned to a cylindrical container where the pin was constrained in a radial groove of the container and would move toward the chamber center when the blade was rotated counterclockwise. This blade rotation caused the blade to approach its midpoint to the chamber center by 1.4 mm, and the chamber was shrunk (left to right in Fig. S6). Conversely, when the blade was rotated clockwise, the pin and blade midpoint moved away from the chamber center, which expanded the chamber (right to left in Fig. S6). To enclose the chamber, we glued to the container a curved ceiling and fluorophilic glass with epoxy (Bob Smith Industries BSI-201). Once the glue was cured, oil and active fluid could be pipetted into the chamber via the loading channel, followed by sealing the channel with epoxy. While the channel was sealed, the chamber remained semi-open because the movable blade required a gap between the ceiling and floor. This gap would allow oil to evaporate and subsequently create air bubbles

that could influence experimental outcomes. To minimize the influence of oil evaporation, we overflowed the gap and blade with oil so that the blade was below the oil surface. This arrangement allowed us to rotate the blade without exposing the chamber to air so the chamber could be shrunk or expanded while filled with oil. This device allowed us to tune the oil layer thickness *in situ* so as to control the formation and deformation of intra-droplet circulatory flows in real time (Fig. 7 and Video S3).

**Design ceiling-adjustable fluidic devices.** To control the shape of the droplet in real time, we needed a milli-fluidic device whose ceiling could be tuned manually. To fabricate such a device, we separated the ceiling from the rest of the fluidic device and attached to the ceiling a handle to manually move the ceiling vertically. We also attached a hanger to hold the ceiling on top of the device chamber (Fig. S7a). To control the vertical position of the ceiling, we designed three platforms with different heights that were placed outside the edge of the device chamber (green, blue, and red) where we could hang the ceiling to adjust its height from  $h = 1$  to 3 mm (Fig. S7b). Finally, because the system was not sealed, the oil could evaporate over time, which might introduce air bubbles that could influence the experimental outcomes. To minimize the influence of oil evaporation, we immersed the system (including the device chamber and ceiling) in an oil bath enclosed in a Petri dish. This device enabled us to control the droplet shape in real time so as to tune the self-organization of intra-droplet flows *in situ* (Fig. 8 and Video S4).

**Data availability:** The data that support the findings of this study are available from the corresponding authors upon reasonable request.

## References

- 1 Palacci, J., Sacanna, S., Steinberg, A. P., Pine, D. J. & Chaikin, P. M. Living Crystals of Light-Activated Colloidal Surfers. *Science* **339**, 936-940 (2013).
- 2 Duclos, G. *et al.* Spontaneous shear flow in confined cellular nematics. *Nature Physics* **14**, 728-732 (2018).
- 3 Herminghaus, S. *et al.* Interfacial mechanisms in active emulsions. *Soft Matter* **10**, 7008-7022 (2014).
- 4 Schaller, V., Weber, C., Semmrich, C., Frey, E. & Bausch, A. R. Polar patterns of driven filaments. *Nature* **467**, 73-77 (2010).
- 5 Farhadi, L., Fermino Do Rosario, C., Debold, E. P., Baskaran, A. & Ross, J. L. Active self-organization of actin-microtubule composite self-propelled rods. *Frontiers in Physics* **6**, 1 (2018).
- 6 Yan, J. *et al.* Reconfiguring active particles by electrostatic imbalance. *Nat Mater* **15**, 1095-1099 (2016).
- 7 Driscoll, M. *et al.* Unstable fronts and motile structures formed by microrollers. *Nature Physics* **13**, 375 (2017).
- 8 Morin, A., Desreumaux, N., Caussin, J.-B. & Bartolo, D. Distortion and destruction of colloidal flocks in disordered environments. *Nat Phys* **13**, 63-67 (2017).
- 9 Soni, V. *et al.* The odd free surface flows of a colloidal chiral fluid. *Nature Physics* **15**, 1188 (2019).
- 10 Blair, D. L. & Kudrolli, A. Collision statistics of driven granular materials. *Physical Review E* **67**, 041301 (2003).
- 11 Wu, K.-T. *et al.* Transition from turbulent to coherent flows in confined three-dimensional active fluids. *Science* **355**, eaal1979 (2017).
- 12 Fan, Y., Wu, K.-T., Aghvami, A., Fraden, S. & Breuer, K. Effects of confinement on the dynamics and correlation scales in active fluids. arXiv:2103.06334 [cond-mat.soft] (2021).
- 13 Suzuki, K., Miyazaki, M., Takagi, J., Itabashi, T. & Ishiwata, S. i. Spatial confinement of active microtubule networks induces large-scale rotational cytoplasmic flow. *Proceedings of the National Academy of Sciences* **114**, 2922-2927 (2017).
- 14 Wioland, H., Woodhouse, F. G., Dunkel, J., Kessler, J. O. & Goldstein, R. E. Confinement Stabilizes a Bacterial Suspension into a Spiral Vortex. *Physical Review Letters* **110**, 268102 (2013).
- 15 Wioland, H., Lushi, E. & Goldstein, R. E. Directed collective motion of bacteria under channel confinement. *New Journal of Physics* **18**, 075002 (2016).
- 16 Doxzen, K. *et al.* Guidance of collective cell migration by substrate geometry. *Integrative Biology* **5**, 1026-1035 (2013).
- 17 Norton, M. M. *et al.* Insensitivity of active nematic liquid crystal dynamics to topological constraints. *Physical Review E* **97**, 012702 (2018).
- 18 Opatthalage, A. *et al.* Self-organized dynamics and the transition to turbulence of confined active nematics. *Proceedings of the National Academy of Sciences* **116**, 4788-4797 (2019).
- 19 Bricard, A. *et al.* Emergent vortices in populations of colloidal rollers. *Nature Communications* **6**, 7470 (2015).
- 20 Morin, A. & Bartolo, D. Flowing active liquids in a pipe: Hysteretic response of polar flocks to external fields. *Physical Review X* **8**, 021037 (2018).
- 21 Delphine, G., David, M., Julien, T. & Bartolo, D. Freezing a flock: Motility-induced phase separation in polar active liquids. *Physical Review X* **9**, 031043 (2019).
- 22 Theillard, M. & Saintillan, D. Computational mean-field modeling of confined active fluids. *Journal of Computational Physics* **397**, 108841 (2019).
- 23 Narayan, V., Ramaswamy, S. & Menon, N. Long-lived giant number fluctuations in a swarming granular Nematic. *Science* **317**, 105-108 (2007).
- 24 Buhl, J. *et al.* From disorder to order in marching locusts. *Science* **312**, 1402-1406 (2006).
- 25 Sokolov, A. & Aranson, I. S. Reduction of viscosity in suspension of swimming bacteria. *Physical Review Letters* **103**, 148101 (2009).

- 26 López, H. M., Gachelin, J., Douarche, C., Auradou, H. & Clément, E. Turning Bacteria Suspensions into Superfluids. *Physical Review Letters* **115**, 028301 (2015).
- 27 Słomka, J. & Dunkel, J. Geometry-dependent viscosity reduction in sheared active fluids. *Physical Review Fluids* **2**, 043102 (2017).
- 28 Hardoüin, J., Guillamat, P., Sagués, F. & Ignés-Mullol, J. Dynamics of ring disclinations driven by active nematic shells. *Frontiers in Physics* **7**(2019).
- 29 Guillamat, P., Hardoüin, J., Prat, B. M., Ignés-Mullol, J. & Sagués, F. Control of active turbulence through addressable soft interfaces. *Journal of Physics: Condensed Matter* **29**, 504003 (2017).
- 30 Guillamat, P., Ignés-Mullol, J. & Sagués, F. Taming active turbulence with patterned soft interfaces. *Nature Communications* **8**, 564 (2017).
- 31 Guillamat, P., Ignés-Mullol, J., Shankar, S., Marchetti, M. C. & Sagués, F. Probing the shear viscosity of an active nematic film. *Physical Review E* **94**, 060602 (2016).
- 32 Chen, S., Gao, P. & Gao, T. Dynamics and structure of an apolar active suspension in an annulus. *Journal of Fluid Mechanics* **835**, 393-405 (2018).
- 33 Gao, T. & Li, Z. Self-driven droplet powered by active nematics. *Physical Review Letters* **119**, 108002 (2017).
- 34 Sanchez, T., Chen, D. T. N., DeCamp, S. J., Heymann, M. & Dogic, Z. Spontaneous motion in hierarchically assembled active matter. *Nature* **491**, 431-434 (2012).
- 35 Zhao, C.-X. Multiphase flow microfluidics for the production of single or multiple emulsions for drug delivery. *Advanced Drug Delivery Reviews* **65**, 1420-1446 (2013).
- 36 Henkin, G., DeCamp, S. J., Chen, D. T. N., Sanchez, T. & Dogic, Z. Tunable dynamics of microtubule-based active isotropic gels. *Philosophical Transactions. Series A, Mathematical, Physical, and Engineering Sciences* **372**, 20140142 (2014).
- 37 Chandrakar, P. *et al.* Microtubule-based active fluids with improved lifetime, temporal stability and miscibility with passive soft materials. arXiv:1811.05026 [cond-mat.soft] (2018).
- 38 Lemma, L. M., Decamp, S. J., You, Z., Giomi, L. & Dogic, Z. Statistical properties of autonomous flows in 2D active nematics. *Soft Matter* **15**, 3264 (2019).
- 39 Bate, T. E., Jarvis, E. J., Varney, M. E. & Wu, K.-T. Collective dynamics of microtubule-based 3D active fluids from single microtubules. *Soft Matter* **15**, 5006-5016 (2019).
- 40 Putzig, E., Redner, G. S., Baskaran, A. & Baskaran, A. Instabilities, defects, and defect ordering in an overdamped active nematic. *Soft Matter* **12**, 3854-3859 (2016).
- 41 Hilitski, F. *et al.* Measuring cohesion between macromolecular filaments one pair at a time: Depletion-induced microtubule bundling. *Physical Review Letters* **114**, 138102 (2015).
- 42 Alabuzhev, A. A. & Lyubimov, D. V. Effect of the contact-line dynamics on the oscillations of a compressed droplet. *Journal of Applied Mechanics and Technical Physics* **53**, 9-19 (2012).
- 43 Wang, D., Duan, H. & Möhwald, H. The water/oil interface: the emerging horizon for self-assembly of nanoparticles. *Soft Matter* **1**, 412-416 (2005).
- 44 Tjhung, E., Marenduzzo, D. & Cates, M. E. Spontaneous symmetry breaking in active droplets provides a generic route to motility. *Proceedings of the National Academy of Sciences* **109**, 12381-12386 (2012).
- 45 Xu, T. *et al.* SOAX: A software for quantification of 3D biopolymer networks. *Scientific Reports* **5**, 9081 (2015).
- 46 Young, Y.-N., Shelley, M. J. & Stein, D. B. The many behaviors of deformable active droplets. *Mathematical Biosciences and Engineering* **18**, 2849-2881 (2021).
- 47 Vicsek, T., Czirók, A., Ben-Jacob, E., Cohen, I. & Shochet, O. Novel type of phase transition in a system of self-driven particles. *Physical Review Letters* **75**, 1226-1229 (1995).
- 48 Hernandez-Ortiz, J. P., Stoltz, C. G. & Graham, M. D. Transport and collective dynamics in suspensions of confined swimming particles. *Physical Review Letters* **95**, 204501 (2005).
- 49 Saintillan, D. & Shelley, M. J. Instabilities, pattern formation, and mixing in active suspensions. *Physics of Fluids* **20**, 123304 (2008).

- 50 Dunkel, J. *et al.* Fluid dynamics of bacterial turbulence. *Physical Review Letters* **110**, 228102 (2013).
- 51 Bratanov, V., Jenko, F. & Frey, E. New class of turbulence in active fluids. *Proceedings of the National Academy of Sciences* **112**, 15048-15053 (2015).
- 52 Toner, J., Tu, Y. & Ramaswamy, S. Hydrodynamics and phases of flocks. *Annals of Physics* **318**, 170-244 (2005).
- 53 Thampi, S. P., Golestanian, R. & Yeomans, J. M. Vorticity, defects and correlations in active turbulence. *Philosophical Transactions of the Royal Society A: Mathematical, Physical and Engineering Sciences* **372**, 20130366 (2014).
- 54 Giomi, L. Geometry and topology of turbulence in active nematics. *Physical Review X* **5**, 031003 (2015).
- 55 Urzay, J., Doostmohammadi, A. & Yeomans, J. M. Multi-scale statistics of turbulence motorized by active matter. *Journal of Fluid Mechanics* **822**, 762-773 (2017).
- 56 Marchetti, M. C. *et al.* Hydrodynamics of soft active matter. *Reviews of Modern Physics* **85**, 1143-1189 (2013).
- 57 Gao, T., Blackwell, R., Glaser, M. A., Betterton, M. D. & Shelley, M. J. Multiscale polar theory of microtubule and motor-protein assemblies. *Physical Review Letters* **114**, 048101 (2015).
- 58 Anderson, D. M., McFadden, G. B. & Wheeler, A. A. Diffuse-interface methods in fluid mechanics. *Annual Review of Fluid Mechanics* **30**, 139-165 (1998).
- 59 Aditi Simha, R. & Ramaswamy, S. Hydrodynamic fluctuations and instabilities in ordered suspensions of self-propelled particles. *Physical Review Letters* **89**, 058101 (2002).
- 60 Mittal, S. & Kumar, B. A stabilized finite element method for global analysis of convective instabilities in nonparallel flows. *Physics of Fluids* **19**, 088105 (2007).
- 61 Bendaraa, A., Charafi, M. M. & Hasnaoui, A. Numerical study of natural convection in a differentially heated square cavity filled with nanofluid in the presence of fins attached to walls in different locations. *Physics of Fluids* **31**, 052003 (2019).
- 62 Cahn, J. W. & Hilliard, J. E. Free energy of a nonuniform system. I. Interfacial free energy. *The Journal of Chemical Physics* **28**, 258-267 (1958).
- 63 Soni, H., Luo, W., Pelcovits, R. A. & Powers, T. R. Stability of the interface of an isotropic active fluid. *Soft Matter* **15**, 6318-6330 (2019).
- 64 Jaros, D. *et al.* Shear treatment of starter culture medium improves separation behavior of streptococcus thermophilus cells. *Engineering in Life Sciences* **18**, 62-69 (2018).
- 65 Diz-Muñoz, A., Fletcher, D. A. & Weiner, O. D. Use the force: Membrane tension as an organizer of cell shape and motility. *Trends in Cell Biology* **23**, 47-53 (2013).
- 66 Needleman, D. & Dogic, Z. Active matter at the interface between materials science and cell biology. *Nature Reviews Materials* **2**, 17048 (2017).
- 67 DeCamp, S. J., Redner, G. S., Baskaran, A., Hagan, M. F. & Dogic, Z. Orientational order of motile defects in active nematics. *Nature Materials* **14**, 1110-1115 (2015).
- 68 Bate, T. E., Jarvis, E. J., Varney, M. E. & Wu, K.-T. Controlling flow speeds of microtubule-based 3D active fluids using temperature. *Journal of Visualized Experiments*, e60484 (2019).
- 69 Ouellette, N. T., Xu, H. & Bodenschatz, E. A quantitative study of three-dimensional Lagrangian particle tracking algorithms. *Experiments in Fluids* **40**, 301-313 (2005).
- 70 Thielicke, W. & Stamhuis, E. J. PIVlab—Towards user-friendly, affordable and accurate digital particle image velocimetry in MATLAB. *Journal of Open Research Software* **2**, e30 (2014).
- 71 Chaikin, P. M. & Lubensky, T. C. *Principles of Condensed Matter Physics*. Vol. 1 (Cambridge University Press, 2000).
- 72 Wang, Z., Ding, H., Lu, G. & Bi, X. Use of a mechanical iris-based fiber optic probe for spatially offset Raman spectroscopy. *Optics letters* **39**, 3790-3793 (2014).

## Acknowledgements

We thank Dr. Zvonimir Dogic for the gift of K401-BCCP-H6 plasmids which were used for expressing the kinesin motor proteins for driving the microtubule-based active fluid. We thank Drs. Yuan-Nan Young and David B. Stein for the insightful discussion on interpreting our experimental data. K.-T.W. acknowledges support from the National Science Foundation (NSF-CBET-2045621). This research was performed using computational resources supported by the Academic & Research Computing Group at Worcester Polytechnic Institute. We acknowledge the Royal Society of Chemistry for adapting the figure from [Bate \*et al.\*](#) on Soft Matter.<sup>39</sup> We acknowledge the Brandeis Materials Research Science and Engineering Center (NSF-MRSEC-DMR-2011486) for use of the Biological Materials Facility. C.-C.C. acknowledges support for the numerical studies from the Headquarters of University Advancement at the National Cheng Kung University, sponsored by the Ministry of Education, Taiwan.

## Author Contributions

Y.-C.C., B.J., C.-C.C., and K.-T.W. performed the research and designed the experiments; Y.-C.C. fabricated the milli-fluidic devices, prepared the samples, tracked the flows, and reconstructed the microtubule-based network structures; Y.-C.C., B.J., and C.-C.C. established the continuum simulation platform on modeling active droplet systems; Y.-C.C. and K.-T.W. organized and analyzed the data; Y.-C.C., C.-C.C., and K.-T.W. wrote the manuscript; K.-T.W. supervised the research. All authors reviewed the manuscript.

## Additional Information

**Competing interests:** The authors declare that they have no competing interests.

**Correspondence** and requests for materials should be addressed to K.-T.W (kwu@wpi.edu). Active fluid simulation questions should be addressed to K.-T.W (kwu@wpi.edu) and C.-C.C (chuehcc@mail.ncku.edu.tw).

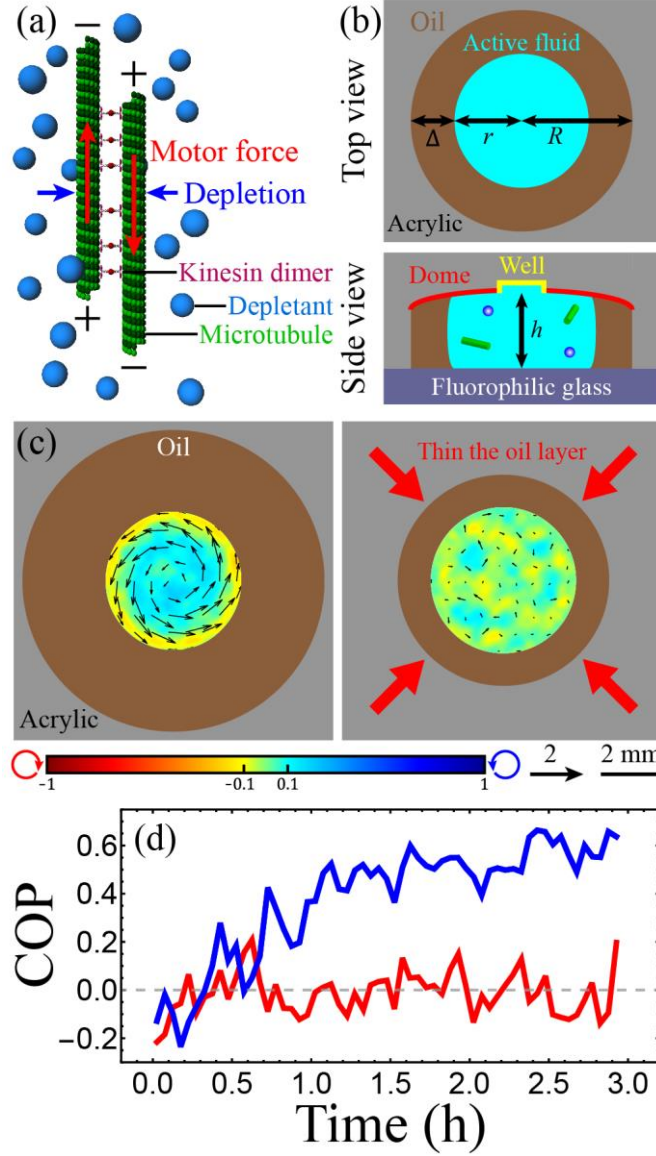


Fig. 1. Flows within a water-in-oil active droplet are influenced by oil configurations. (a) Schematic of mutually sliding microtubule pairs. Microtubules were bundled by depletion (blue arrows) and subsequently bridged by kinesin dimers that slid apart pairs of anti-parallel microtubules (red arrows). This figure was adapted from Bate *et al.*<sup>39</sup> (b) Schematic of compressing an active droplet using an acrylic–glass fluidic device. The device ceiling was curved into a dome-like geometry (red curve), and a well was drilled (radius 1 mm, depth 0.2 mm) on top of the dome (yellow curve). The curved ceiling caused the active droplet to remain stationary at the dome center. (c) An active droplet ( $r \approx 2.4$  mm,  $h \approx 2$  mm) confined in an oil layer whose thickness was  $\Delta \approx 2.6$  mm developed a circulatory flow (left). The circulatory flow was suppressed by decreasing the oil layer thickness to  $\Delta \approx 1.1$  mm (right). Black arrows represented time-averaged velocity flow fields normalized by the flow mean speed. The color maps represent normalized vorticity distributions, with red and blue tone colors representing clockwise and counterclockwise vorticities, respectively. Videos of the flows in both systems are available in Video S2. (d) Evolution of circulation order parameter (COP) of flows within the active droplets in c (blue: left; red: right).

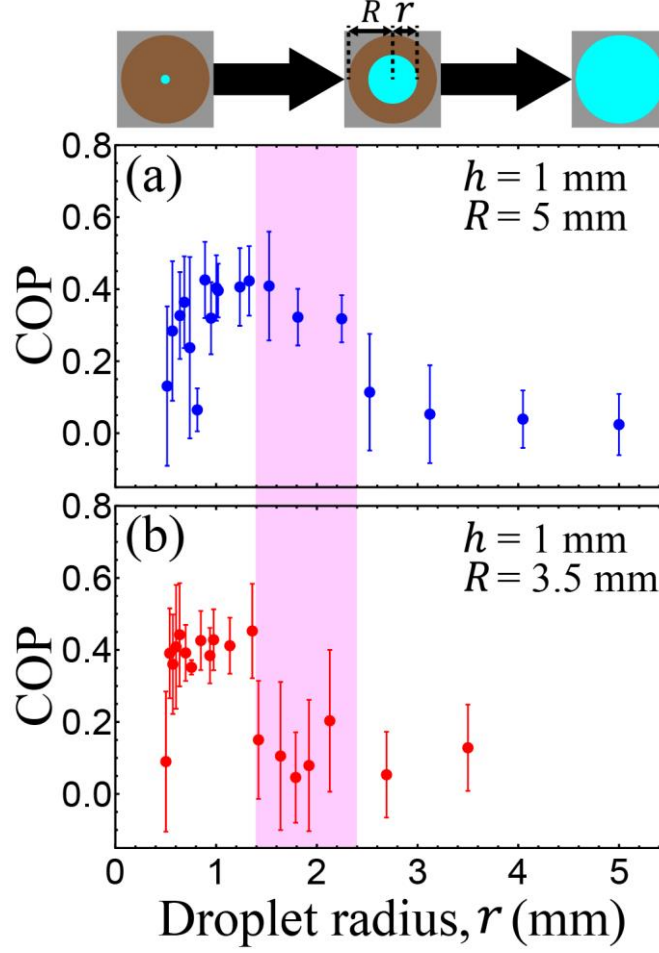


Fig. 2. The intra-droplet circulatory flows depended on the dimensions of the droplets and oil. (a) The droplets immersed in an oil of radius  $R = 5$  mm developed circulatory flows when their radii were  $r \lesssim 2.4$  mm. Enlarging the droplets above this limit suppressed the formation of the circulatory flows. (b) However, such critical radius was altered when the oil was shrunken to a radius of  $R = 3.5$  mm. In this case, the circulation transition was shifted to  $r \approx 1.4$  mm, highlighted by the shaded pink area. The shift implied that the intra-droplet circulatory flows were affected by the oil dimensions and by the droplet shapes. Each error bar represents the standard deviation of the time-averaged circulation order parameter.



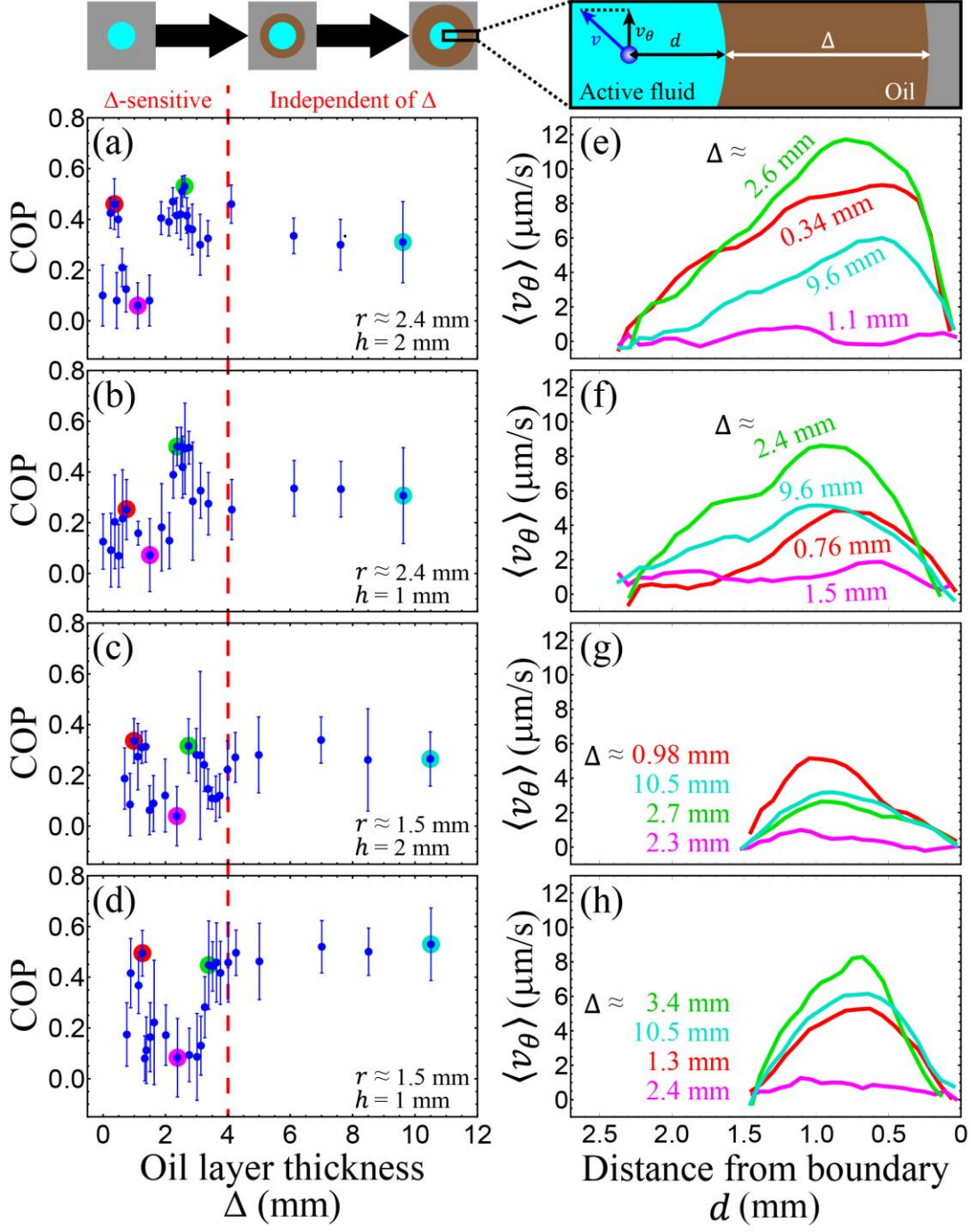


Fig. 3. Intra-droplet circulatory flows depended on the thicknesses of the extra-droplet oil layers  $\Delta$ . (a-d) The circulation order parameter as a function of  $\Delta$  for four different droplets. Across these droplets, the intra-droplet flows varied rapidly when the oil layer was thinner than  $\sim 4$  mm (red dashed line), whereas the oil layers thicker than this limit did not affect intra-droplet flows. Each error bar represents the standard deviation of the time-averaged circulation order parameter. (e-h) Flow profiles of azimuthal velocities  $v_\theta$  taken at droplet midplanes. Each curve represents the averaged flow velocity of the data point shaded in the same color in the same row of a-d. These curves demonstrate that varying the thickness of the oil layer without contacting the droplets altered the structures and rates of intra-droplet flows.

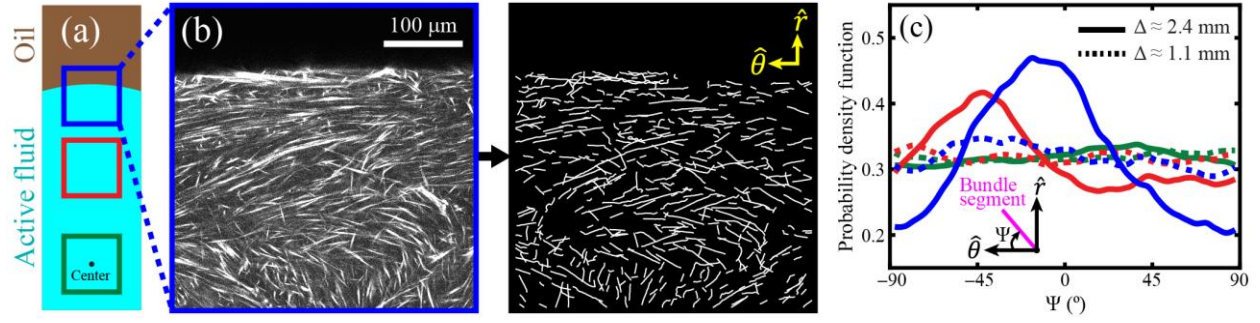


Fig. 4. Intra-droplet circulatory flows were accompanied with the formation of a weak nematic layer in the microtubule network structure near the water–oil interface. The droplet had a radius of  $r \approx 2.4$  mm and a height of  $h = 1$  mm. (a) Microtubule network structures were imaged with a confocal microscope at three different locations: around the water–oil interface (blue),  $\sim 400$   $\mu\text{m}$  from the interface (red), and at the droplet center (green). (b) The confocal image of the microtubule network at the droplet midplane (left) was analyzed with the snake algorithm to extract the network structure (right).<sup>45</sup> The droplet was immersed in an oil layer whose thickness was  $\Delta \approx 2.4$  mm and developed an intra-droplet circulatory flow. (c) Orientational distributions of microtubule bundles when intra-droplet flows were circulating (solid,  $\Delta \approx 2.4$  mm) and not circulating (dashed,  $\Delta \approx 1.1$  mm). Blue, red, and green represent the different locations within the droplet as indicated in a. Circulating flows were accompanied with aligned microtubule bundles tilting from  $\sim 15^\circ$  (solid blue curve) to  $45^\circ$  (solid red curve) as away from the water–oil interface, whereas in non-circulating flows, the bundles oriented isotopically.

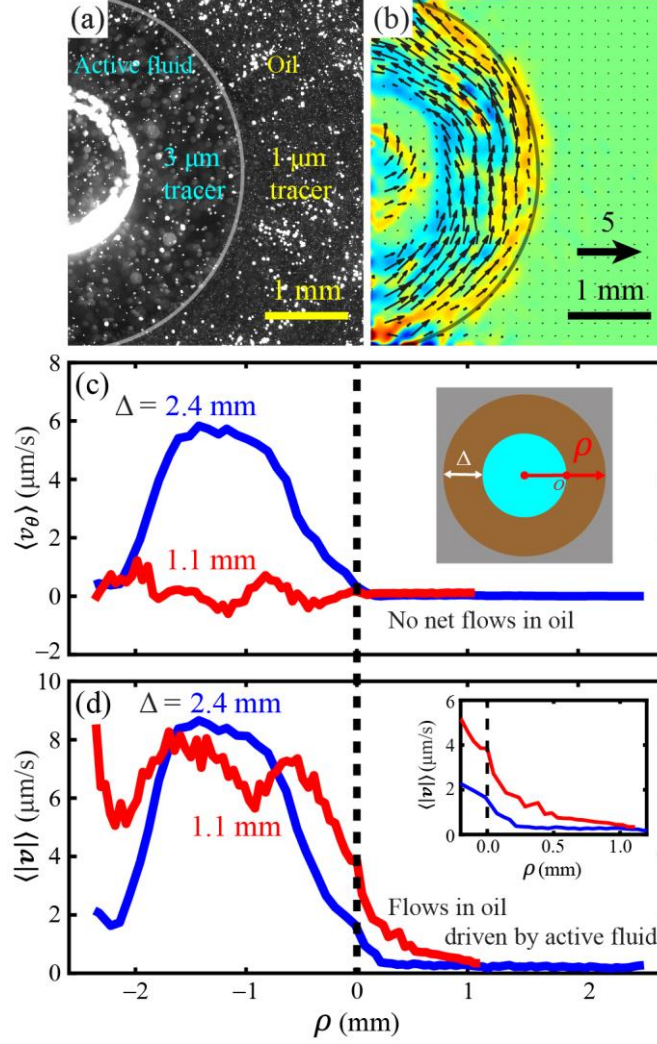


Fig. 5. Active fluid induced chaotic flows in oil. (a) Micrographs of an active droplet ( $r \approx 2.4$  mm,  $h = 1$  mm) immersed in oil ( $\Delta \approx 2.4$  mm). To track the flows, the active fluid and oil were doped with tracers. The gray curve represents a water–oil interface. (b) Time-averaged normalized velocity field and vorticity map revealed an intra-droplet circulatory flow immersed in an idling oil. The velocity field and vorticity map were plotted as in Fig. 1c. (c) Flow profiles of azimuthal velocities taken at midplanes of two droplets. The droplets had the same geometry ( $r \approx 2.4$  mm,  $h = 1$  mm) but were immersed in different oil layers ( $\Delta$ ). The thicker layer supported intra-droplet circulatory flows (blue curve), whereas in the thinner layer the flows were chaotic (red curve). However, regardless of how the active fluids flowed within the droplets, the oil developed no net flow. Dashed line indicates the water–oil interface. Inset: Schematic of horizontal axis  $\rho$  of the plot.  $\rho > 0$  represents the oil regime;  $\rho < 0$  represents the droplet regime. (d) Flow speed profiles in the corresponding droplets in c. Both profiles extended across the water–oil interfaces into the oil regime ( $\rho > 0$ ), demonstrating that the active fluid flows near the interface drove the nearby oils. Inset: Close-up of the profiles near the water–oil interface.

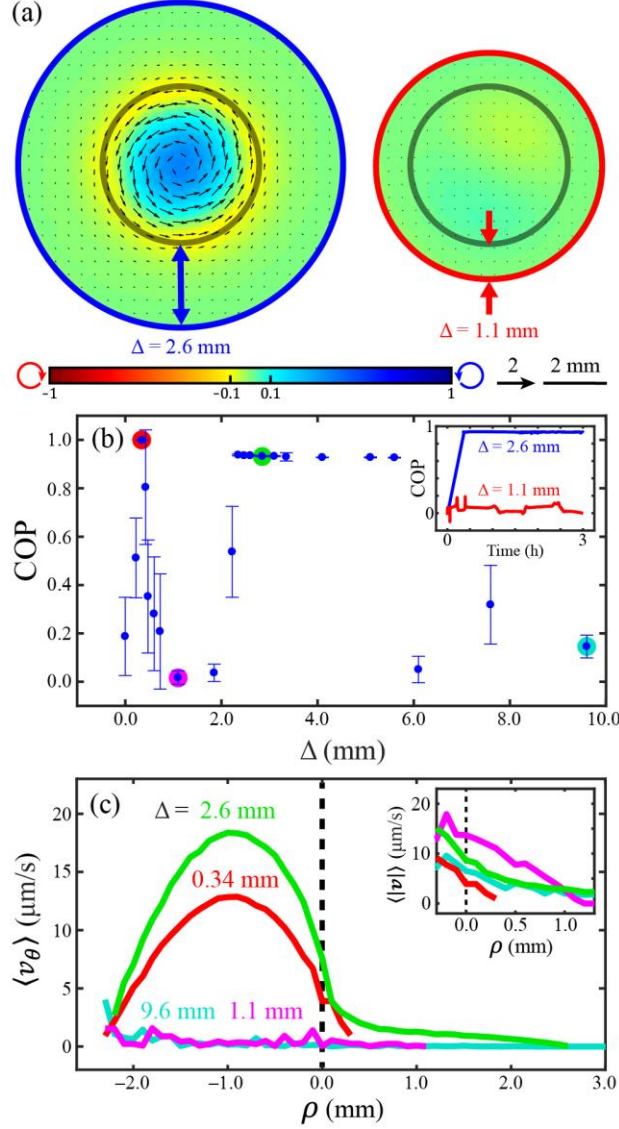


Fig. 6. Simulating compressed water-in-oil droplets using continuum active fluid equations. (a) Time-averaged velocity fields and vorticity maps taken at the midplanes of compressed droplets ( $r = 2.4$  mm,  $h = 2$  mm) immersed in oil layers of different thicknesses ( $\Delta$ ). The velocities and vorticities were plotted as in Fig. 1c. Gray curves represent the water-oil interfaces; blue and red curves represent the no-slip boundaries. Droplets immersed in a thicker oil layer ( $\Delta = 2.6$  mm) developed circulatory flows (left), whereas in a thinner oil layer ( $\Delta = 1.1$  mm) the circulatory flows were suppressed (right). (b) Circulation order parameter as a function of the layer thickness of the oil that immerses a compressed droplet ( $r = 2.4$  mm,  $h = 2$  mm). The intra-droplet flows were sensitive to oil layer thickness when the thicknesses were thinner than  $\sim 2.2$  mm. Each error bar represents the standard deviation of the time-averaged circulation order parameter. Inset: Evolution of circulation order parameters within the corresponding droplets in a. (c) Flow profiles of azimuthal velocities  $v_\theta$  taken at droplet midplanes. The horizontal axis is the same as in Figs. 5c&d. Each curve represents the averaged flow velocity of the data points shaded in the same color in b. Dashed lines represent the water-oil interface. These flow profiles demonstrated that intra-droplet circulatory flows induced a thin layer (0.3–2 mm thick) of circulatory flow in oil near the interface, indicating that flows within and outside the interface were coupled. Inset: Flow speed profiles near the droplet interface.

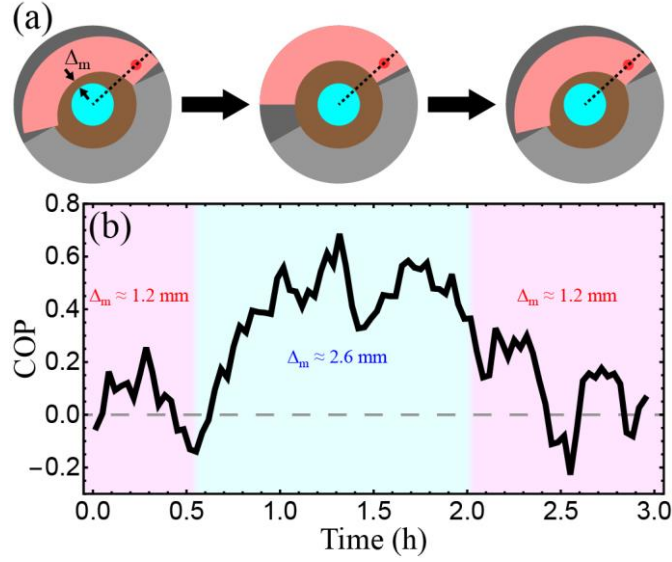


Fig. 7. Manipulate the oil layer thickness to trigger and suppress intra-droplet circulatory flows in real time. (a) Schematics of manipulating the oil layer thickness with a movable wall (pink). The wall was anchored to a cylindrical container (gray) by a pin (red dot) that could only move radially (dashed black lines). Moving the pin toward the container center rotated the wall counterclockwise and reduced the minimum oil layer thickness ( $\Delta_m$ ), whereas pushing the pin outward rotated the wall clockwise and increased the oil layer thickness. The device enabled tuning the oil layer thickness by manually moving the pin. The device design that realized such wall manipulation is shown in Fig. S6. (b) The evolution of circulation order parameter of flows in a droplet ( $r \approx 2.4$  mm,  $h = 2$  mm) revealed that increasing the minimum oil layer thickness ( $\Delta_m$ ) regulated the chaotic flows into circulatory flows (left pink to middle cyan areas). Conversely, decreasing the minimum oil layer thickness suppressed the circulatory flows (middle cyan to right pink areas). A video of manipulating the formation and deformation of intra-droplet circulatory flows using the wall-movable device is available in Video S3.



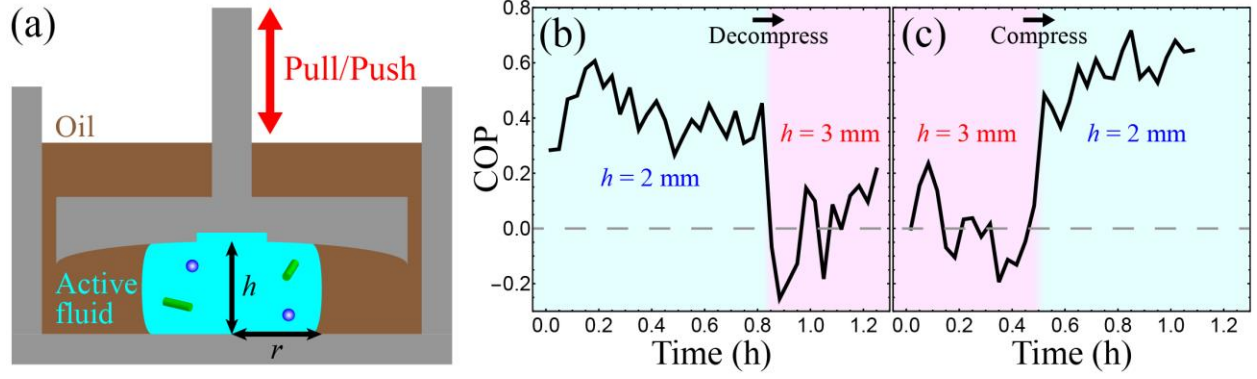


Fig. 8. Suppress and trigger intra-droplet circulatory flows in real time using a ceiling-tunable device. (a) Schematic of compressing a droplet with a movable ceiling to manually tune the droplet height. Because the droplet volume was conserved, decreasing the droplet height  $h$  enlarged the droplet radius  $r$  and vice versa. (b) Circulatory flows within a droplet were suppressed by decompressing the droplet (cyan to pink areas). The decompression reduced the droplet radius from  $r \approx 2.0$  to 1.7 mm. (c) Conversely, compressing the droplet regulated the chaotic flows into circulatory flows (pink to cyan areas). The compression expanded the droplet radius from  $r \approx 1.7$  to 2.0 mm. A video of manipulating the formation and deformation of the circulatory flows using a ceiling-tunable device is available in Video S4.

# Supplemental information:

## Flow coupling between active and passive fluids across interfaces of compressed active droplets

Yen-Chen Chen<sup>1</sup>, Brock Jolicoeur<sup>2</sup>, Chih-Che Chueh<sup>3</sup>, and Kun-Ta Wu<sup>1,2,4,\*</sup>

<sup>1</sup>Department of Mechanical Engineering, Worcester Polytechnic Institute, Worcester, Massachusetts 01609, USA

<sup>2</sup>Department of Physics, Worcester Polytechnic Institute, Worcester, Massachusetts 01609, USA

<sup>3</sup>Department of Aeronautics and Astronautics, National Cheng Kung University, Tainan 701, Taiwan

<sup>4</sup>The Martin Fisher School of Physics, Brandeis University, Waltham, Massachusetts 02454, USA

### Influence of the ceiling geometry on the intra-droplet active fluid behavior

Compressed active droplets have been reported to self-propel,<sup>1-4</sup> preventing us from observing intra-droplet flows for long durations with a fixed observation window. As such, we fixed the droplet by curving the ceiling of the fluidic device into a dome-like shape and then drilled a thin well at the dome center to reinforce droplet immobilization (Fig. S1a). However, these shape modifications changed the droplet geometries, which might influence the self-organization of active fluids in droplets. Here, we examined

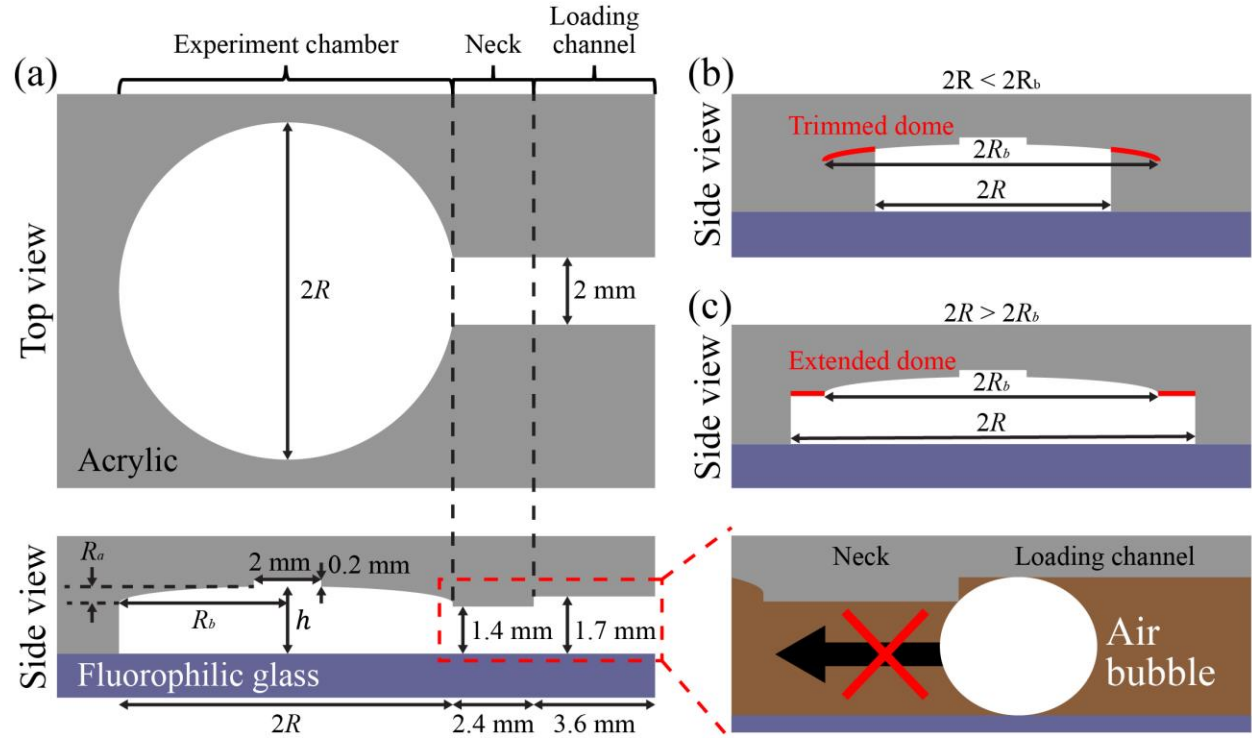


Fig. S1: Design of milli-fluidic devices. (a) The device contained a cylinder-like chamber to contain the oil and droplet, which were loaded via the loading channel. The channel was connected to the chamber via a neck to keep air bubbles away from the chamber (close-up). To fix the droplet in the chamber center, the chamber ceiling was curved into a half-oblate spheroidal shape whose semi-axes were  $R_a$  and  $R_b$ , along with a thin well at the ceiling center. Close-up: An air-in-oil bubble in the loading channel could not spontaneously enter the chamber due to the smaller opening of the neck. (b) To fit a half-spheroidal dome into a smaller chamber ( $2R < 2R_b$ ), the dome was trimmed (red curves). (c) Conversely, to match a dome to a larger chamber ( $2R > 2R_b$ ), the dome was extended horizontally (red lines).

how the intra-droplet active fluid flows were influenced by the geometric parameters of the ceilings (i.e., the well dimensions and dome shape).

**Influence of well dimensions.** First, we investigated the role of the well geometry on intra-droplet flows. The well was cylindrical; its geometry depended on its height (or depth) and radius. To examine how these parameters influenced intra-droplet flows, we measured the circulation order parameter within a droplet while varying the well radii (Fig. S2a) and depths (Fig. S2b) separately. Across our explored parameters, our measured circulation order parameters remained steady (fluctuating between 0.4 and 0.6), suggesting that the well geometry did not play a significant role in the formation of intra-droplet circulatory flows. In

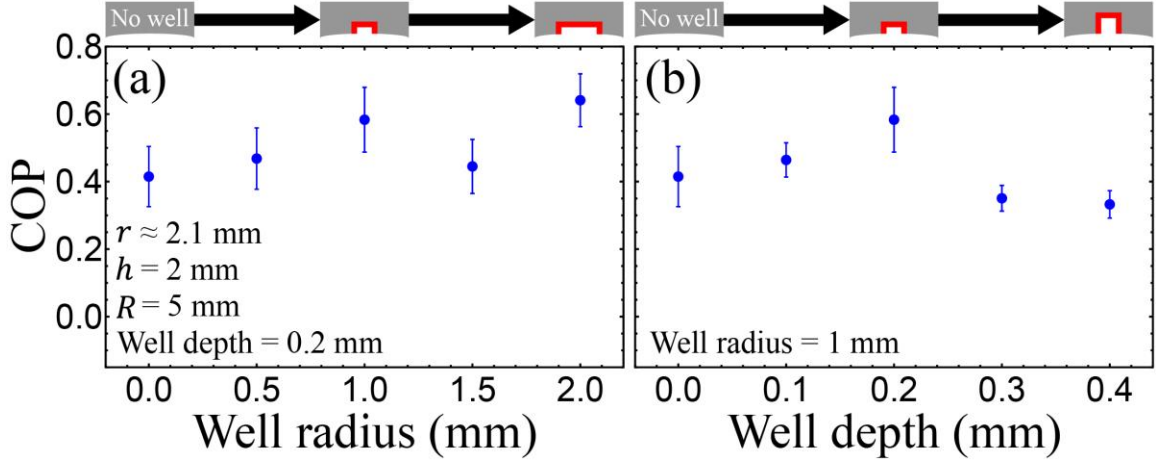


Fig. S2: Intra-droplet circulatory flows were not significantly influenced by the well dimensions. Geometries of the half-spheroidal domes were fixed ( $R_a = 0.5$  mm,  $R_b = 5$  mm). Varying either the well radii (a) or the well depths (b) did not significantly alter the circulation order parameter, suggesting that the wells did not play a substantial role in intra-droplet flows. In this study, we chose a well with a radius of 1 mm and a depth of 0.2 mm to reinforce the droplet immobilization. Each error bar represents the standard deviation of the time-averaged circulation order parameter.

this study, we chose a well geometry (depth 0.2 mm, radius 1 mm) whose COP could not be distinguished from the case without a well (within error bars). We expected that imposing this well to ceilings could reinforce droplet immobilization while minimizing the well's influence on intra-droplet active fluid flows.

**Influence of dome shape.** Next, we characterized how the intra-droplet active fluid flows were influenced by the dome shape. The dome was shaped into a half-oblate spheroid whose geometry depended on its vertical and horizontal semi-axes (Fig. S1a). To characterize how the dome geometry influenced intra-droplet circulatory flows, we systematically varied the vertical semi-axes  $R_a = 0.25$ – $1.5$  mm while maintaining the horizontal semi-axes  $R_b = R = 5$  mm (Fig. S1a) and then measured the corresponding circulation order parameters of intra-droplet flows (Fig. S3). Our measurements showed that circulatory flows persisted when the vertical semi-axes were shorter than  $\sim 1$  mm ( $\text{COP} > 0.4$ ); lengthening the semi-axes longer than this limit weakened the formation of circulatory flows ( $\text{COP} \leq 0.4$ ). This result suggested that the dome shape influences the formation of intra-droplet flows, but this influence was limited to largely curved dome ( $R_a \gtrsim 1$  mm). To minimize this dome-induced influence while immobilizing the droplets, we adopted half-spheroidal domes with a vertical semi-axis of  $R_a = 0.25$ – $0.5$  mm and a horizontal semi-axis of  $R_b = 3.5$ – $5$  mm.



In summary, observing the intra-droplet active fluid flows over a long duration required compressing the droplets with a curved ceiling. However, the curved ceiling influenced the intra-droplet fluid flows. To

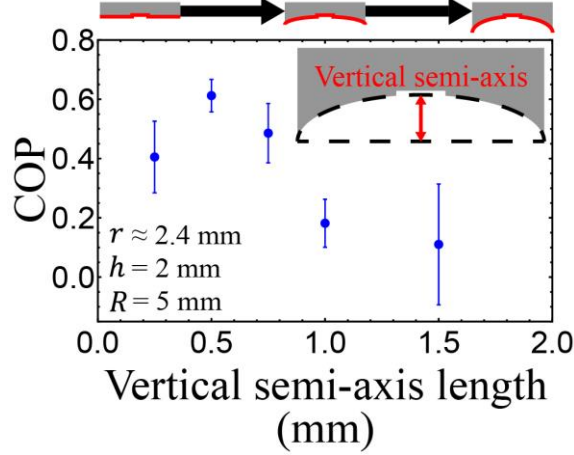


Fig. S3: Intra-droplet circulatory flows were influenced by the dome shape. The well geometry was fixed (radius 1 mm, depth 0.5 mm), and the domes were half-oblate spheroids with a horizontal semi-axis of 5 mm and vertical semi-axes ranging from 0.25 to 1.5 mm. Lengthening the vertical semi-axes increased the dome curvature. Such increases in curvature sharpened the droplet shape and suppressed development of circulatory flows when vertical semi-axes were longer than  $\sim 1$  mm ( $\text{COP} \leq 0.4$ ); for the semi-axes shorter than this limit, circulatory flows were stable, suggesting that domes with a larger curvature had a greater influence on intra-droplet flows. Thus, we selected a slightly curved dome ( $R_a = 0.5$  mm,  $R_b = 5$  mm) to compress the droplets. Each error bar represents the standard deviation of the time-averaged circulation order parameter.

minimize this influence, we chose the ceiling shape that would not suppress development of circulatory flows but was sufficiently curved to fix the droplets. This arrangement provided a stationary active droplet that allowed us to investigate how the formation of intra-droplet circulatory flows was controlled by other geometric parameters such as the droplet radii and oil layer thickness (Figs. 1–3).

### Modeling active droplet systems with a continuum active fluid simulation

To test whether an existing active fluid model was capable of describing the influences of water–oil coupling on intra-droplet active fluid flows,<sup>3,5–25</sup> we adopted the active droplet model established by Gao *et al.* because this model closely matched our experimental system, which involved a microtubule-based active fluid immersed in a water-in-oil droplet.<sup>3</sup> The model applied a cylindrical no-slip boundary (radius  $R$ , height  $h$ ) with a curved ceiling, which was identical to the confinement geometry in the experiments (Fig. 1b). The boundary was filled with oil (density  $\rho_o$ , dynamic viscosity  $\mu_o$ ), immersing a concentric cylindrical active fluid (radius  $r$ , density  $\rho_a$ , dynamic viscosity  $\mu_a$ ) modeled as a compressed water-in-oil droplet. The water–oil interface was modeled as variations of a phase function:

$$c = H\left(1 - \frac{\sqrt{x^2 + y^2}}{r}\right), \quad (\text{S1})$$

where  $H$  is the Heaviside step function with  $c(\sqrt{x^2 + y^2} \leq r) = 1$  representing the active fluid and  $c(\sqrt{x^2 + y^2} > r) = 0$  representing the oil. To speed up the simulations and to match our experimental arrangement for immobilizing the droplets, we fixed the water–oil interface so the phase function was kept constant, rather than evolving as in the Cahn–Hilliard model.<sup>26</sup> The phase function varied at the water–oil

interface, which induced interfacial tension forces  $\mathbf{T} \equiv (\gamma K/\epsilon)\nabla c$ , where  $\gamma$  is the interfacial tension,  $\epsilon$  is the interface thickness, and  $K \equiv c(c-1)(c-1/2) - \epsilon^2 \nabla^2 c$  is the chemical potential that characterizes the phase variation within the interfacial region.<sup>27</sup> Within the interface, active fluid generated active stress  $\sigma_a$  to induce self-driven flows  $\mathbf{u}$  in incompressible fluids ( $\nabla \cdot \mathbf{u} = 0$ ) that were governed by the Navier–Stokes equation:

$$\rho \left( \frac{\partial \mathbf{u}}{\partial t} + \mathbf{u} \cdot \nabla \mathbf{u} \right) = \nabla \cdot [-p\mathbf{I} + \mu(\nabla \mathbf{u} + \nabla \mathbf{u}^T)] + \mathbf{F}, \quad (\text{S2})$$

where  $\rho$  is the fluid density,  $p$  is the fluid pressure,  $\mu$  is the dynamic viscosity of the fluid, and  $\mathbf{F} \equiv \mathbf{T} + \nabla \cdot \sigma_a$  is the net body force. Calculating the net body force required determining the active stress, which was exerted by the extensile microtubule-based bundles in the experiment. Here, we modeled each extensile bundle as a self-elongating rod whose center of mass is  $\mathbf{x} = (x, y, z)$  orienting at  $\mathbf{p} = (\sin \theta \cos \varphi, \sin \theta \sin \varphi, \cos \theta)$ . The configurations of these rods were described using a mean-field probability distribution function  $\Psi(\mathbf{x}, \mathbf{p}, t)$  normalized as  $\int_{\mathbf{p}} \Psi d\mathbf{p} = 1$ . To conserve probability, the distribution function satisfied the Smoluchowski equation as:

$$\frac{\partial \Psi}{\partial t} + \nabla \cdot (\dot{\mathbf{x}}\Psi) + \nabla_{\mathbf{p}} \cdot (\dot{\mathbf{p}}\Psi) = 0, \quad (\text{S3})$$

where  $\nabla_{\mathbf{p}} \equiv \partial(\mathbf{I} - \mathbf{p}\mathbf{p})/\partial \mathbf{p}$  is the surface derivative on the unit sphere.<sup>10,12,28,29</sup> Considering these rods were only advected by fluid flows, the translational flux of the rods was determined as  $\dot{\mathbf{x}} = \mathbf{u} - D_T \nabla \ln \Psi$ , where  $D_T$  is the translational diffusion coefficient. The rotational flux induced by the fluid velocity gradient is  $\dot{\mathbf{p}} = (\mathbf{I} - \mathbf{p}\mathbf{p}) \cdot (\nabla \mathbf{u} + 2\zeta \mathbf{D}) \cdot \mathbf{p} - D_R \nabla_{\mathbf{p}} \ln \Psi$ , where  $\zeta$  is the mean-field torque strength and  $D_R$  is the rotational diffusion coefficient.<sup>12,30–32</sup> These equations describe the coupling between the fluid flows and the rods' translational and rotational distributions, but solving these equations was computationally expensive. To reduce the computation load, the Smoluchowski equation was coarse-grained as

$$\frac{\partial \mathbf{D}}{\partial t} - D_T \Delta \mathbf{D} + \mathbf{u} \cdot \nabla \mathbf{D} = 4\zeta(\mathbf{D} \cdot \mathbf{D} - \mathbf{D} : \mathbf{S}) + \nabla \mathbf{u} \cdot \mathbf{D} + \mathbf{D} \cdot \nabla \mathbf{u}^T - 2\mathbf{E} : \mathbf{S} - 6D_R \left( \mathbf{D} - \frac{\mathbf{I}}{3} \right), \quad (\text{S4})$$

where  $\mathbf{E} \equiv \frac{\nabla \mathbf{u} + \nabla \mathbf{u}^T}{2}$  is the strain rate tensor,  $\mathbf{D} \equiv \int_{\mathbf{p}} \mathbf{p}\mathbf{p}\Psi d\mathbf{p}$  is the orientational average of the second-moment tensor of the rod orientation  $\mathbf{p}\mathbf{p}$ , and  $\mathbf{S} \equiv \mathbf{D}\mathbf{D}$ .<sup>29,33</sup> The coarse-grained Smoluchowski equation allowed for determining the configuration of the self-elongating rods, which generated an active stress that was modeled to be proportional to the local rod orientational order:<sup>21</sup>  $\sigma_a = \alpha c \mathbf{D}$ , where  $\alpha$  is the activity coefficient, with  $\alpha > 0$  representing contracting rods and  $\alpha < 0$  representing elongating rods, and  $\mathbf{D} \equiv \int_{\mathbf{p}} \mathbf{p}\mathbf{p}\Psi d\mathbf{p}$  represents the orientational order of the rods.<sup>34</sup> The active stress drove the fluids whose flows were determined via the Navier–Stokes equation (Eq. (S2), which in return rearranged the rod configurations and reformulated the active stress via the coarse-grained Smoluchowski equation (Eq. (S4). Both equations formed a feedback loop to simultaneously evolve the fluid flows, rod configurations, and active stresses.

To solve these equations and to develop a simulation platform for modeling our active droplet systems, we expressed both equations in explicit forms that were fed into COMSOL Multiphysics<sup>TM</sup>, which solved the equations using the finite element method.<sup>35–39</sup> To feed in the Navier–Stokes equation (Eq. (S2), we utilized the template of the 3D laminar flow model in the software. This template considers incompressible fluids ( $\nabla \cdot \mathbf{u} = 0$ ) governed by the Navier–Stokes equation with a net body force which could be expressed as

$$\mathbf{F} = \begin{bmatrix} F_x \\ F_y \\ F_z \end{bmatrix} = \alpha \begin{bmatrix} c \left( \frac{\partial D_{xx}}{\partial x} + \frac{\partial D_{yx}}{\partial y} + \frac{\partial D_{zx}}{\partial z} \right) + D_{xx} \frac{\partial c}{\partial x} + D_{yx} \frac{\partial c}{\partial y} + D_{zx} \frac{\partial c}{\partial z} \\ c \left( \frac{\partial D_{xy}}{\partial x} + \frac{\partial D_{yy}}{\partial y} + \frac{\partial D_{zy}}{\partial z} \right) + D_{xy} \frac{\partial c}{\partial x} + D_{yy} \frac{\partial c}{\partial y} + D_{zy} \frac{\partial c}{\partial z} \\ c \left( \frac{\partial D_{xz}}{\partial x} + \frac{\partial D_{yz}}{\partial y} + \frac{\partial D_{zz}}{\partial z} \right) + D_{xz} \frac{\partial c}{\partial x} + D_{yz} \frac{\partial c}{\partial y} + D_{zz} \frac{\partial c}{\partial z} \end{bmatrix} + \frac{\gamma K}{\epsilon} \begin{bmatrix} \frac{\partial c}{\partial x} \\ \frac{\partial c}{\partial y} \\ \frac{\partial c}{\partial z} \end{bmatrix}, \quad (\text{S5})$$

where  $\frac{\partial c}{\partial x_i} = \frac{-x_i \delta(r - \sqrt{x^2 + y^2})}{\sqrt{x^2 + y^2}}$ ,  $K = c(c - 1) \left( c - \frac{1}{2} \right) - \epsilon^2 \left[ \delta'(r - \sqrt{x^2 + y^2}) - \frac{\delta(r - \sqrt{x^2 + y^2})}{\sqrt{x^2 + y^2}} \right]$ , and  $\delta$  is the Dirac delta function. To include the coarse-grained Smoluchowski equation (Eq. (S4)), we rearranged the equation as:

$$\frac{\partial \mathbf{D}}{\partial t} - D_T \Delta \mathbf{D} + \begin{bmatrix} u_x \\ u_y \\ u_z \end{bmatrix} \cdot \nabla \mathbf{D} = - \begin{bmatrix} a_{xx} & a_{xy} & a_{xz} \\ a_{yx} & a_{yy} & a_{yz} \\ a_{zx} & a_{zy} & a_{zz} \end{bmatrix} \circ \mathbf{D} + \begin{bmatrix} f_{xx} & f_{xy} & f_{xz} \\ f_{yx} & f_{yy} & f_{yz} \\ f_{zx} & f_{zy} & f_{zz} \end{bmatrix}, \quad (\text{S6})$$

where

$$\begin{aligned} a_{xx} &= 4\zeta(D_{xx}^2 + D_{yy}^2 + D_{zz}^2 + 2D_{xy}D_{yx} + 2D_{xz}D_{zx} + 2D_{yz}D_{zy} - D_{xx}) \\ &\quad + 2 \left[ (D_{xx} - 1) \frac{\partial u_x}{\partial x} + D_{yy} \frac{\partial u_y}{\partial y} + D_{zz} \frac{\partial u_z}{\partial z} \right] + (D_{xy} + D_{yx}) \left( \frac{\partial u_x}{\partial y} + \frac{\partial u_y}{\partial x} \right) \\ &\quad + (D_{xz} + D_{zx}) \left( \frac{\partial u_x}{\partial z} + \frac{\partial u_z}{\partial x} \right) + (D_{yz} + D_{zy}) \left( \frac{\partial u_y}{\partial z} + \frac{\partial u_z}{\partial y} \right) + 6D_R, \\ a_{yy} &= 4\zeta(D_{xx}^2 + D_{yy}^2 + D_{zz}^2 + 2D_{xy}D_{yx} + 2D_{xz}D_{zx} + 2D_{yz}D_{zy} - D_{yy}) \\ &\quad + 2 \left[ D_{xx} \frac{\partial u_x}{\partial x} + (D_{yy} - 1) \frac{\partial u_y}{\partial y} + D_{zz} \frac{\partial u_z}{\partial z} \right] + (D_{xy} + D_{yx}) \left( \frac{\partial u_x}{\partial y} + \frac{\partial u_y}{\partial x} \right) \\ &\quad + (D_{xz} + D_{zx}) \left( \frac{\partial u_x}{\partial z} + \frac{\partial u_z}{\partial x} \right) + (D_{yz} + D_{zy}) \left( \frac{\partial u_y}{\partial z} + \frac{\partial u_z}{\partial y} \right) + 6D_R, \\ a_{zz} &= 4\zeta(D_{xx}^2 + D_{yy}^2 + D_{zz}^2 + 2D_{xy}D_{yx} + 2D_{xz}D_{zx} + 2D_{yz}D_{zy} - D_{zz}) \\ &\quad + 2 \left[ D_{xx} \frac{\partial u_x}{\partial x} + D_{yy} \frac{\partial u_y}{\partial y} + (D_{zz} - 1) \frac{\partial u_z}{\partial z} \right] + (D_{xy} + D_{yx}) \left( \frac{\partial u_x}{\partial y} + \frac{\partial u_y}{\partial x} \right) \\ &\quad + (D_{xz} + D_{zx}) \left( \frac{\partial u_x}{\partial z} + \frac{\partial u_z}{\partial x} \right) + (D_{yz} + D_{zy}) \left( \frac{\partial u_y}{\partial z} + \frac{\partial u_z}{\partial y} \right) + 6D_R, \\ a_{xy} = a_{yx} &= 4\zeta(D_{xx}^2 + D_{yy}^2 + D_{zz}^2 + 2D_{xy}D_{yx} + 2D_{xz}D_{zx} + 2D_{yz}D_{zy} - D_{xx} - D_{yy}) \\ &\quad + 2 \left[ \left( D_{xx} - \frac{1}{2} \right) \frac{\partial u_x}{\partial x} + \left( D_{yy} - \frac{1}{2} \right) \frac{\partial u_y}{\partial y} + D_{zz} \frac{\partial u_z}{\partial z} \right] + (D_{xy} + D_{yx}) \left( \frac{\partial u_x}{\partial y} + \frac{\partial u_y}{\partial x} \right) \\ &\quad + (D_{xz} + D_{zx}) \left( \frac{\partial u_x}{\partial z} + \frac{\partial u_z}{\partial x} \right) + (D_{yz} + D_{zy}) \left( \frac{\partial u_y}{\partial z} + \frac{\partial u_z}{\partial y} \right) + 6D_R, \end{aligned}$$

$$\begin{aligned}
a_{xz} = a_{zx} = & 4\zeta(D_{xx}^2 + D_{yy}^2 + D_{zz}^2 + 2D_{xy}D_{yx} + 2D_{xz}D_{zx} + 2D_{yz}D_{zy} - D_{xx} - D_{zz}) \\
& + 2\left[\left(D_{xx} - \frac{1}{2}\right)\frac{\partial u_x}{\partial x} + D_{yy}\frac{\partial u_y}{\partial y} + \left(D_{zz} - \frac{1}{2}\right)\frac{\partial u_z}{\partial z}\right] + (D_{xy} + D_{yx})\left(\frac{\partial u_x}{\partial y} + \frac{\partial u_y}{\partial x}\right) \\
& + (D_{xz} + D_{zx})\left(\frac{\partial u_x}{\partial z} + \frac{\partial u_z}{\partial x}\right) + (D_{yz} + D_{zy})\left(\frac{\partial u_y}{\partial z} + \frac{\partial u_z}{\partial y}\right) + 6D_R,
\end{aligned}$$

$$\begin{aligned}
a_{yz} = a_{zy} = & 4\zeta(D_{xx}^2 + D_{yy}^2 + D_{zz}^2 + 2D_{xy}D_{yx} + 2D_{xz}D_{zx} + 2D_{yz}D_{zy} - D_{yy} - D_{zz}) \\
& + 2\left[D_{xx}\frac{\partial u_x}{\partial x} + \left(D_{yy} - \frac{1}{2}\right)\frac{\partial u_y}{\partial y} + \left(D_{zz} - \frac{1}{2}\right)\frac{\partial u_z}{\partial z}\right] + (D_{xy} + D_{yx})\left(\frac{\partial u_x}{\partial y} + \frac{\partial u_y}{\partial x}\right) \\
& + (D_{xz} + D_{zx})\left(\frac{\partial u_x}{\partial z} + \frac{\partial u_z}{\partial x}\right) + (D_{yz} + D_{zy})\left(\frac{\partial u_y}{\partial z} + \frac{\partial u_z}{\partial y}\right) + 6D_R,
\end{aligned}$$

$$f_{xx} = 4\zeta(D_{xy}D_{yx} + D_{xz}D_{zx}) + (D_{xy} + D_{yx})\frac{\partial u_y}{\partial x} + (D_{xz} + D_{zx})\frac{\partial u_z}{\partial x} + 2D_R,$$

$$f_{yy} = 4\zeta(D_{xy}D_{yx} + D_{yz}D_{zy}) + (D_{xy} + D_{yx})\frac{\partial u_x}{\partial y} + (D_{yz} + D_{zy})\frac{\partial u_z}{\partial y} + 2D_R,$$

$$f_{zz} = 4\zeta(D_{xz}D_{zx} + D_{yz}D_{zy}) + (D_{xz} + D_{zx})\frac{\partial u_x}{\partial z} + (D_{yz} + D_{zy})\frac{\partial u_y}{\partial z} + 2D_R,$$

$$f_{xy} = 4\zeta D_{xz}D_{zy} + D_{xx}\frac{\partial u_x}{\partial y} + D_{xz}\frac{\partial u_z}{\partial y} + D_{yy}\frac{\partial u_y}{\partial x} + D_{zy}\frac{\partial u_z}{\partial x},$$

$$f_{yx} = 4\zeta D_{yz}D_{zx} + D_{xx}\frac{\partial u_x}{\partial y} + D_{zx}\frac{\partial u_z}{\partial y} + D_{yy}\frac{\partial u_y}{\partial x} + D_{yz}\frac{\partial u_z}{\partial x},$$

$$f_{xz} = 4\zeta D_{xy}D_{yz} + D_{xx}\frac{\partial u_x}{\partial z} + D_{xy}\frac{\partial u_y}{\partial z} + D_{yz}\frac{\partial u_y}{\partial x} + D_{zz}\frac{\partial u_z}{\partial x},$$

$$f_{zx} = 4\zeta D_{yx}D_{zy} + D_{xx}\frac{\partial u_x}{\partial z} + D_{yx}\frac{\partial u_y}{\partial z} + D_{zy}\frac{\partial u_y}{\partial x} + D_{zz}\frac{\partial u_z}{\partial x},$$

$$f_{yz} = 4\zeta D_{xz}D_{yx} + D_{yx}\frac{\partial u_x}{\partial z} + D_{yy}\frac{\partial u_y}{\partial z} + D_{xz}\frac{\partial u_x}{\partial y} + D_{zz}\frac{\partial u_z}{\partial y}, \text{ and}$$

$$f_{zy} = 4\zeta D_{xy}D_{zx} + D_{xy}\frac{\partial u_x}{\partial z} + D_{yy}\frac{\partial u_y}{\partial z} + D_{zx}\frac{\partial u_x}{\partial y} + D_{zz}\frac{\partial u_z}{\partial y}.$$

The rearranged equation was fed into the software using the built-in stabilized convective diffusion equation. Solving these equations numerically required defining the system domains and the associated boundary conditions. As such, we imported 3D computer-aided designs (SOLIDWORKS) identical to the geometries of our experimental containers (Fig. 1b) as system domains and then imposed to the domain surfaces a no-slip boundary condition:  $\mathbf{u} = \mathbf{0}$ . Because the rods were limited within the domain, we also imposed a no-flux boundary condition:  $\mathbf{n} \cdot \nabla \Psi = 0$ , or equivalently  $\mathbf{n} \cdot \nabla \mathbf{D} = \mathbf{0}$ , where  $\mathbf{n}$  represents the unit vectors normal to domain surfaces, without enforcing rod orientations at boundaries.<sup>29,33</sup> To evolve the fluid flows and rod configurations, we initialized the fluids as quiescent fluids ( $\mathbf{u} = \mathbf{0}$ ) under uniform pressure ( $p = 0$ )

with uniformly suspended isotropic rods whose translational and orientational distributions were perturbed with 15 random modes.<sup>10,11</sup>

$$\Psi(\mathbf{x}, \mathbf{p}, 0) = \frac{1}{4\pi} \left[ 1 + \sum_{i=1}^{15} \epsilon_i P_i(\mathbf{p}) \cos(\mathbf{k}_i \cdot \mathbf{x} + \varsigma_i) \right], \quad (\text{S7})$$

which determined the initial second moment tensor as

$$\mathbf{D}(\mathbf{x}, 0) = \int_{\mathbf{p}} \mathbf{p} \mathbf{p} \Psi(\mathbf{x}, \mathbf{p}, 0) d\mathbf{p} = \frac{\mathbf{I}}{3} + \frac{1}{4\pi} \sum_{i=1}^{15} \epsilon_i \cos(\mathbf{k}_i \cdot \mathbf{x} + \varsigma_i) \int_{\mathbf{p}} \mathbf{p} \mathbf{p} P_i(\mathbf{p}) d\mathbf{p}, \quad (\text{S8})$$

where  $\epsilon_i$  is the random numbers in  $[-0.01, 0.01]$ ,  $\mathbf{k}_i$  is the random wave numbers whose components are random numbers in  $[\pi, 15\pi] \text{ mm}^{-1}$ ,  $\varsigma_i$  is the random phases in  $[0, 2\pi]$ , and  $P_i(\mathbf{p}) = \sum_{j=1}^3 \sum_{k=1}^4 \xi_{ijk} g_k^j$  is the random polynomials of sine and cosine with  $\xi_{ijk}$  as the random numbers in  $[0, 1]$  and  $g_k$  defined as:  $g_1 \equiv \sin(\theta)$ ,  $g_2 \equiv \cos(\theta)$ ,  $g_3 \equiv \sin(\varphi)$ , and  $g_4 \equiv \cos(\varphi)$ . The initialized second moment tensor and fluid flow were evolved for 3 hours of model time using the selected model parameters (Table S1). The resulting flow field  $\mathbf{u}$  was analyzed to determine the circulation order parameters and flow profiles (Fig. 6), which were compared with experimental outcomes (Figs. 3&5).

Symbol	Description	Value
$\alpha$	Activity coefficient ( $\alpha < 0$ : enlogating rods; $\alpha > 0$ : contracting rods).	−50 Pa
$\gamma$	Water–oil interfacial tension at 25 °C.	0.072 N/m
$\epsilon$	Thickness of the water–oil interface of droplets immersed in oil.	50 $\mu\text{m}$
$D_T$	Translational diffusion coefficient of rods.	0.011 $\text{m}^2/\text{s}$
$D_R$	Rotational diffusion coefficient of rods.	10 $\text{s}^{-1}$
$\zeta$	Mean-field torque strength on rods induced by flow velocity gradient.	100 $\text{s}^{-1}$
$\rho_a$	Density of active fluid (96% water) at 25 °C.	997 $\text{kg}/\text{m}^3$
$\rho_o$	Density of oil (hydrofluoroether, 3M Novec 7500) at 25 °C. <sup>40</sup>	1614 $\text{kg}/\text{m}^3$
$\mu_a$	Dynamic viscosity of active fluid (96% water) at 25 °C.	0.00089 Pa·s
$\mu_o$	Dynamic viscosity of oil (hydrofluoroether, 3M Novec 7500) at 25 °C. <sup>40</sup>	0.00124 Pa·s

Table S1: Descriptions and values of parameters used in the simulations. The activity coefficient, translational diffusion coefficient, and rotational diffusion coefficient were selected to match the flow speeds in the simulation with those in the experiments ( $\sim 10 \mu\text{m}/\text{s}$ ). The mean-field torque strength was selected to be four times larger than the rotational diffusion coefficient ( $\zeta > 4D_R$ ) to enforce strong flow alignment of the rods. The water–oil interfacial tension was approximated as the surface tension of water at 25 °C.<sup>41</sup>

### Active fluid–oil flow coupling from the perspective of a cross-correlation function

Our simulation platform revealed that flows of active fluid were coupled to those of oil across the water–oil interface with a millimeter-scale coupling length (Fig. 6c). To gain deeper insight into this coupling, we analyzed the normalized same-time velocity–velocity spatial cross-correlation function between the flows of active fluid and oil:

$$C(\Delta X) \equiv \frac{\langle \mathbf{v}_o(\mathbf{x} + \Delta \mathbf{X}, t) \cdot \mathbf{v}_w(\mathbf{x}, t) \rangle_{\mathbf{x}, t}}{\langle \mathbf{v}_o(\mathbf{x}, t) \cdot \mathbf{v}_w(\mathbf{x}, t) \rangle_{\mathbf{x}, t}}, \quad (\text{S9})$$

where  $\mathbf{v}_o$  is the 3D flow velocity field in oil,  $\mathbf{v}_w$  is this in active fluid, and  $\langle \cdot \rangle_{\mathbf{x}, t}$  indicates averaging over time and active fluid region. The correlation function of confined active fluid is reportedly influenced by boundary geometries.<sup>42–45</sup> Therefore, to minimize the influence from the top and bottom boundaries ( $z = 0$  and  $h$ ), we only considered flows at the midplane ( $z = h/2$ ). To address the flow coupling near the water–oil interface, we only considered the active fluid flows that were within 100  $\mu\text{m}$  of the interface ( $|r - x| \leq 100 \mu\text{m}$ ). To reveal the interaction range between active fluid and oil, we averaged the correlation function over the orientation:

$$C(\Delta X) \equiv \langle C(\Delta \mathbf{X}) \rangle_{|\Delta \mathbf{X}| = \Delta X}. \quad (\text{S10})$$

Our analysis revealed that the correlation function decayed nearly exponentially with increasing distance between an active fluid element and oil element ( $C \sim e^{-\Delta X/L}$ , where  $L$  is the correlation length), suggesting that the active fluid–oil interaction is short ranged (Fig. S4a). To quantify the interaction range, we extracted the correlation length  $L$  and then analyzed the correlation length as a function of oil layer thickness (Fig. S4b). Our analysis revealed that the correlation length linearly increased with the oil layer thickness ( $L \approx \Delta$ ), eventually reaching saturation ( $L \approx 1.4 \text{ mm}$ ). The linear increase indicated that the active fluid flows were coupled to the oil flows throughout the oil region. Hence, the geometry of the oil affected the active fluid flows, which was consistent with our observation that the circulation order parameter in the active fluid changed rapidly with the oil layer thickness when the thickness was small ( $\Delta < 2 \text{ mm}$  in Fig. 6b). The

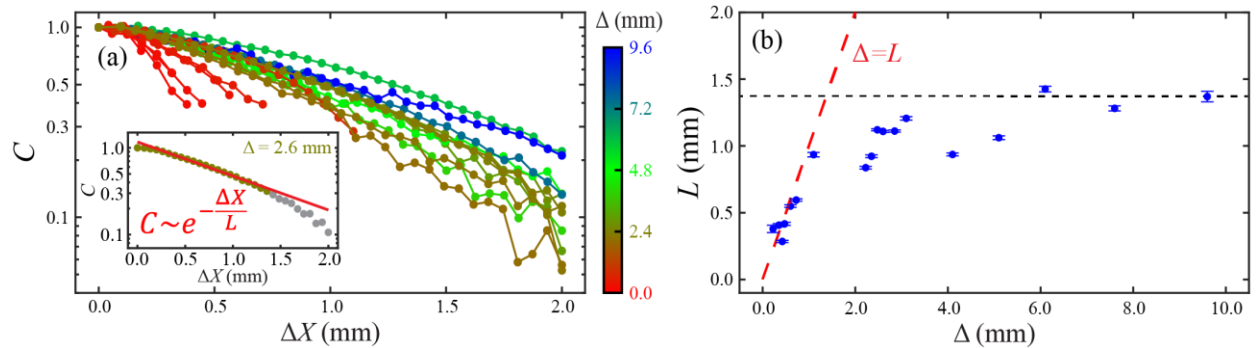


Fig. S4: Simulations revealed that flows inside and outside the droplets were correlated with a correlation length that increased with the oil layer thickness. The droplet had the same geometry as in Fig. 6 ( $r = 2.4 \text{ mm}$ ,  $h = 2 \text{ mm}$ ). (a) Normalized same-time velocity–velocity spatial cross-correlation functions between active fluid near the water–oil interface (within 100  $\mu\text{m}$ ) and oil for various oil layer thicknesses  $\Delta$ . The correlation functions decayed with increasing distance between active fluid element and the oil element ( $\Delta X$ ). Inset: The initial decay length (defined as the correlation length)  $L$  of the correlation function was extracted by excluding the correlation data below 0.3 (gray dots) and fitting the remaining correlation data (olive dots) to an exponential function:  $e^{-\Delta X/L}$  with  $L$  as a fitting parameter (red line). (b) The correlation length increased linearly with the oil layer thickness (dashed red line) before reaching saturation (black dashed line). Error bars represent uncertainties in fitting the correlation function to an exponential function (inset in a).

saturation indicated that the range of active fluid–oil interaction has an upper limit ( $\sim 1.4$  mm) above which the motion of oil elements did not affect the active fluid. Such an indication was consistent with our observation that the circulation order parameter in the active fluid was independent of the oil layer thickness when the oil layer was sufficiently thick ( $\Delta > 2$  mm in Fig. 6b). Moreover, the scale of the analyzed correlation length ( $\sim 1.4$  mm; Fig. S4b) was consistent with the observed coupling length ( $\sim 1$  mm; Fig. 6c). This consistency supported our assertion that active fluid and oil interact across the water–oil interface with a millimeter-scale interaction range.

### Formation of two-dimensional nematic layers at water–oil interfaces

The microtubule-based active fluid system is known to deposit its microtubules onto the water–oil interface and form 2D active nematics.<sup>46–54</sup> Our active fluid was encapsulated in a water-in-oil droplet, which created water–oil interfaces, so the intra-droplet microtubules were expected to gather at the interface and develop 2D active nematics. To verify our expectation, we prepared a compressed water-in-oil active droplet ( $r \approx 2.4$  mm,  $h = 1$  mm,  $\Delta \approx 2.4$  mm) and imaged microtubules at the water–oil interface of the droplet bottom using fluorescence microscopy (Fig. S5a). The microtubules were labeled with Alexa 647, which can be imaged with a Cy5 filter cube (excitation: 618–650nm, emission: 670–698 nm, Semrock, 96376) (Fig. S5b&c). Our observation showed that microtubules formed a layer of nematics at the water–oil interface with multiple motile plus- and minus-half defects.<sup>16,23,24,49–51,53–56</sup> These motile microtubule-based defects at the interface served as a dynamic boundary that confined the active fluid. To examine whether such a dynamic boundary was coupled to the self-organization of the confined active fluid, we simultaneously imaged microtubules at the bottom interface and at the droplet midplane for 15 minutes and then analyzed microtubule motion with the particle image velocimetry algorithm to extract the velocity fields of the microtubule motions (arrows in Fig. S5b).<sup>57</sup> The velocity fields enabled us to analyze the circulation order parameter as a function of time (Fig. S5d). Our analyses showed that microtubules at the midplane

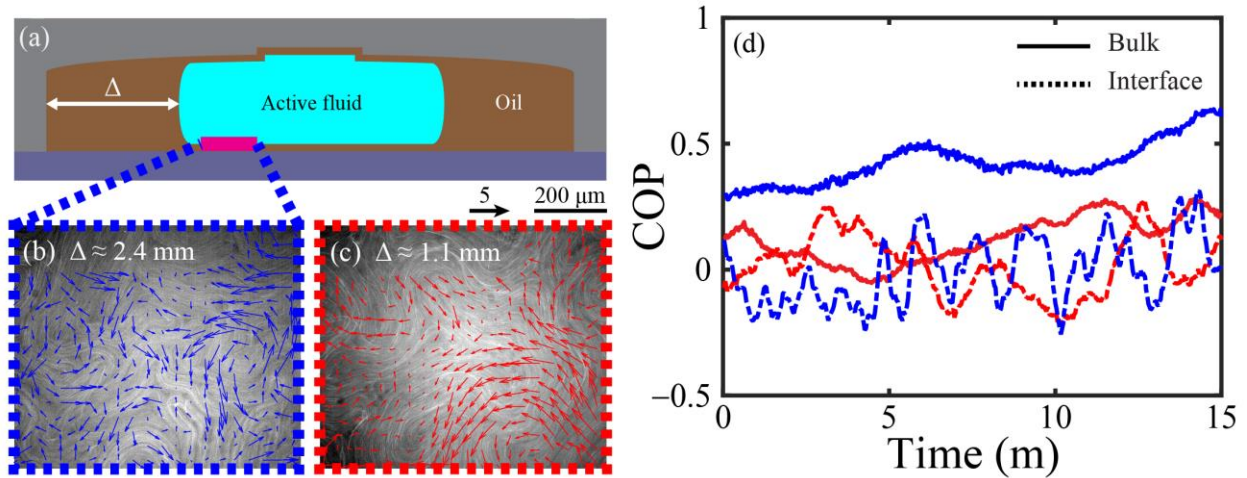


Fig. S5: Microtubules self-organized into a layer of motile nematics at water–oil interfaces whose flows were not influenced by microtubule flows in bulk. (a) Schematic of imaging the nematic layer at the water–oil interface at the droplet bottom (magenta line). (b&c) Confocal micrographs of the microtubule-based nematic layer at the water–oil interfaces of droplets that had the same shape ( $r = 2.4$  mm,  $h = 1$  mm) but were immersed in different oil layers ( $\Delta$ ). The arrows are normalized velocity fields of corresponding instant nematic flows. (d) Evolution of circulation order parameters of microtubule flows in bulk (midplanes; solid curves) and at water–oil interface (dashed curves). Blue curves represent the droplet in b; red curves in c. In b, the microtubules in bulk developed circulatory flows ( $\text{COP} \approx 0.5$ , solid blue curve), whereas in c, the bulk flows were chaotic (red solid curve). However, regardless of how the microtubules flowed in bulk, the microtubule-based nematics flowed chaotically (dashed curves).

developed circulatory flows ( $\text{COP} \approx 0.5$ , solid blue curve), whereas at the bottom interface the microtubule flows were chaotic ( $|\text{COP}| \lesssim 0.2$ , dashed blue curve). This comparison indicated that the microtubule flows in bulk and at the interface were not coupled. To confirm such bulk–interface decoupling, we repeated the experiments but immersed the droplet in a thinner oil layer ( $\Delta \approx 1.1$  mm, Fig. S5c). The thinner layer did not support circulatory flows in the droplet bulk ( $|\text{COP}| \lesssim 0.2$ , solid red curve in Fig. S5d); simultaneously, the microtubule motion at the interface remained chaotic ( $|\text{COP}| \lesssim 0.2$ , dashed red curve). Our analyses showed that microtubule motions at the interface of the droplet bottom were not related to microtubule motions in bulk. However, our analyses did not suggest that the dynamic boundary was disconnected from the self-organization of intra-droplet flows. We have shown that oil near the interface flowed faster when the active fluid flowed chaotically than when the active fluid developed circulatory flows (Fig. 5d), which implies that the microtubule motion at the droplet sides was coupled to the intra-droplet fluid flows. Unveiling such a coupling required further studies to monitor the microtubules at the droplet lateral interfaces. Here, we demonstrated that microtubules developed 2D active nematics at the water–oil interfaces of droplets and that nematic motions at the droplet bottom interfaces were decoupled from flows in the droplet bulk.



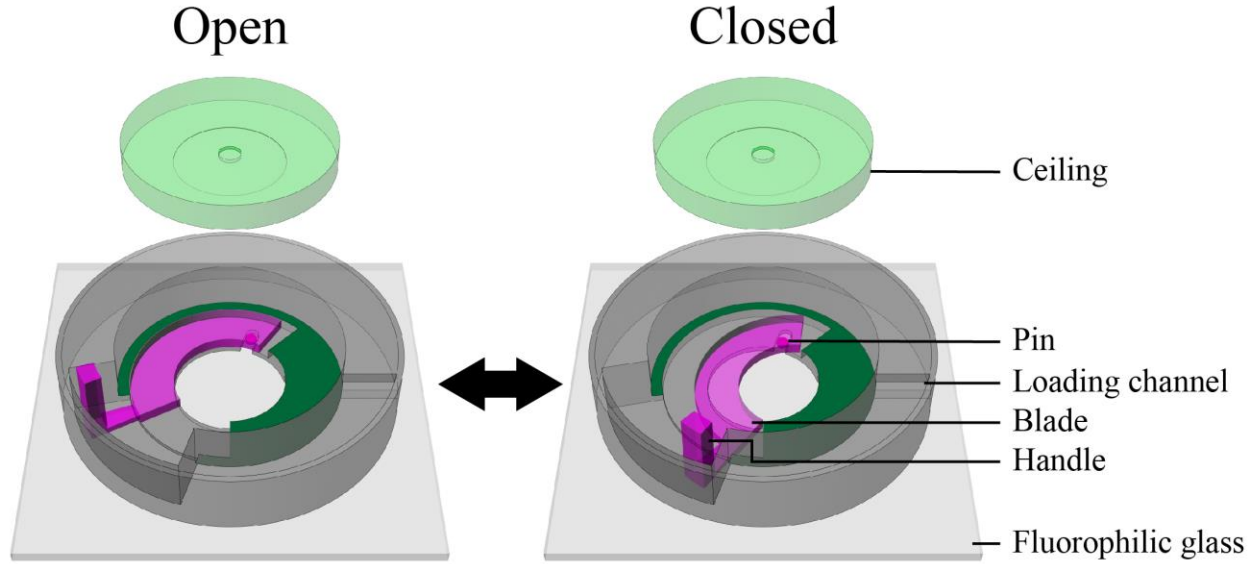


Fig. S6: Schematics of the wall-movable milli-fluidic device used to manipulate the layer thicknesses of the oil that immersed an active droplet. The device consisted of a container (gray) that had a cylindrical chamber (radius  $R = 5$  mm, height 1.5 mm), a curved ceiling ( $R_a = 0.5$  mm,  $R_b = R = 5$  mm, light green) that sat on the dark-green platform to enclose the chamber, and a blade (pink) that altered the oil layer thickness. The blade comprised a blade body whose inner side wall served as a movable boundary of the chamber, a pin that was constrained in a groove of the container, and a handle used to manually rotate the blade body around the pin during experiments. Rotating the blade counterclockwise slid the pin inward, shifted the blade midpoint toward chamber center by 1.4 mm, and thus shrank the chamber (left to right). Conversely, rotating the blade clockwise slid the pin outward, shifted the blade midpoint away from the chamber center, and expanded the chamber (right to left). This device enabled real-time tuning of the layer thickness of the oil that immersed the droplets.

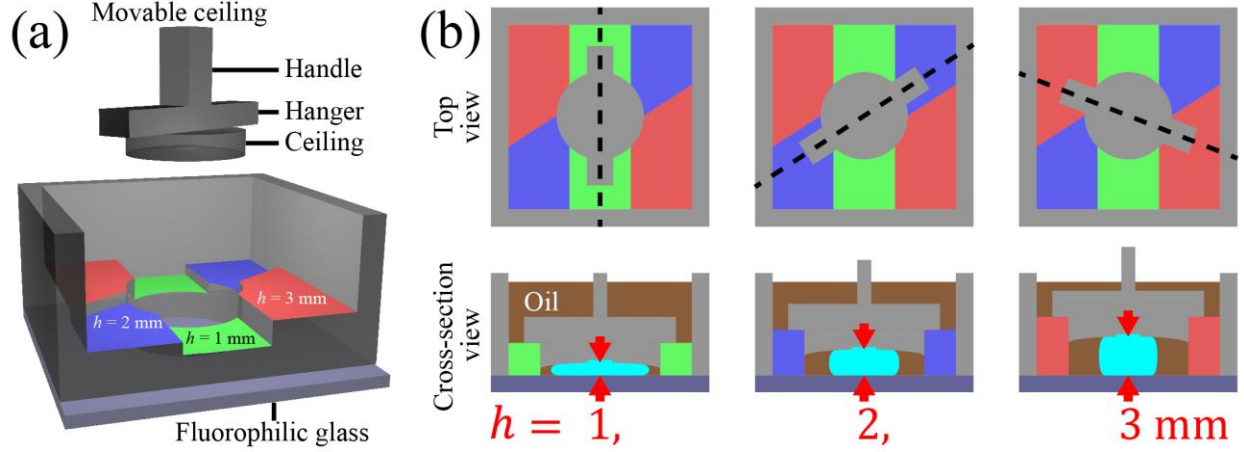


Fig. S7: Design of a ceiling-movable milli-fluidic device for manually compressing a droplet. (a) Schematic of the device design. We designed the droplet to be compressed in a cylindrical well (radius  $R = 5$  mm) with a movable ceiling. The ceiling consisted of a handle used to manually adjust the ceiling height, a curved ceiling ( $R_a = 0.5$  mm,  $R_b = 5$  mm) used to fix the droplet at the ceiling center, and a hanger that was designed to sit on the colored platforms (green, blue, and red) to place the ceiling at various heights ( $h$ ). To ensure that the droplet remained in oil while moving the ceiling, we submerged the central well, ceiling, and platforms in oil that was held in a cubical container (gray walls). The front side of the container was transparentized to visualize the platform design. (b) Schematic demonstrations of compressing a water-in-oil droplet (cyan) utilizing the colored platforms. From left to right, the ceiling hanger was placed on green, blue, and red platforms, causing the ceiling to compress the droplet with the heights of  $h = 1$ , 2, and 3 mm, respectively. The dashed lines indicate cross-section planes.

Video S1: Circulation of microtubule-based active fluids confined in a water-in-oil droplet. The droplet was compressed into a cylinder-like geometry with a height of  $h = 2$  mm and a radius of  $r \approx 1$  mm. The time stamp is hour: minute: second.

Video S2: The oil layer thickness controlled the formation of circulatory flows in droplets, visualized by tracer movements. The droplet was compressed into a cylinder-like geometry with a height of  $h = 2$  mm and a radius of  $r \approx 2.4$  mm, immersed in an oil bath. When the oil had a layer thickness of  $\Delta \approx 2.6$  mm, the circulatory flows developed. Decreasing the oil layer thickness to  $\Delta \approx 1.1$  mm suppressed the circulatory flows. The time stamp is hour: minute: second.

Video S3: Manipulate the formation of intra-droplet circulatory flows using a wall-movable fluidic device. The circulatory flows developed after the blade was moved away from the droplet, which increased the oil layer thickness from 1.2 to 2.6 mm (00:33:54–00:34:01). By contrast, the circulatory flows faded away after the blade approached the droplet, which decreased the oil layer thickness from 2.6 to 1.2 mm (02:00:51–02:00:54). The time stamp is hour: minute: second.

Video S4: Control the formation of intra-droplet circulatory flows using a ceiling-adjustable fluidic device. The circulatory flows were suppressed by lifting the ceiling from  $h = 2$  to 3 mm (00:50:18–00:50:38), whereas the circulatory flows were triggered by lowering the ceiling from  $h = 3$  to 2 mm (00:30:20–00:30:52). During these time frames, the image brightness was oversaturated by the room light that was needed to manually lower or lift the ceiling. The time stamp is hour: minute: second.

## References

- 1 Sanchez, T., Chen, D. T. N., DeCamp, S. J., Heymann, M. & Dogic, Z. Spontaneous motion in hierarchically assembled active matter. *Nature* **491**, 431-434 (2012).
- 2 Tjhung, E., Marenduzzo, D. & Cates, M. E. Spontaneous symmetry breaking in active droplets provides a generic route to motility. *Proceedings of the National Academy of Sciences* **109**, 12381-12386 (2012).
- 3 Gao, T. & Li, Z. Self-driven droplet powered by active nematics. *Physical Review Letters* **119**, 108002 (2017).
- 4 Loisy, A., Eggers, J. & Liverpool, T. B. Tractionless self-propulsion of active drops. *Physical Review Letters* **123**, 248006 (2019).
- 5 Vicsek, T., Czirók, A., Ben-Jacob, E., Cohen, I. & Shochet, O. Novel type of phase transition in a system of self-driven particles. *Physical Review Letters* **75**, 1226-1229 (1995).
- 6 Chaté, H., Ginelli, F., Grégoire, G., Peruani, F. & Raynaud, F. Modeling collective motion: variations on the Vicsek model. *The European Physical Journal B* **64**, 451-456 (2008).
- 7 Saintillan, D. & Shelley, M. J. Orientational order and instabilities in suspensions of self-locomoting rods. *Physical Review Letters* **99**, 058102 (2007).
- 8 Hernandez-Ortiz, J. P., Stoltz, C. G. & Graham, M. D. Transport and collective dynamics in suspensions of confined swimming particles. *Physical Review Letters* **95**, 204501 (2005).
- 9 Saintillan, D. & Shelley, M. J. Active suspensions and their nonlinear models. *Comptes Rendus Physique* **14**, 497-517 (2013).
- 10 Saintillan, D. & Shelley, M. J. Instabilities, pattern formation, and mixing in active suspensions. *Physics of Fluids* **20**, 123304 (2008).
- 11 Saintillan, D. & Shelley, M. J. Instabilities and pattern formation in active particle suspensions: Kinetic theory and continuum simulations. *Physical Review Letters* **100**, 178103 (2008).
- 12 Gao, T., Blackwell, R., Glaser, M. A., Betterton, M. D. & Shelley, M. J. Multiscale polar theory of microtubule and motor-protein assemblies. *Physical Review Letters* **114**, 048101 (2015).
- 13 Chen, S., Gao, P. & Gao, T. Dynamics and structure of an apolar active suspension in an annulus. *Journal of Fluid Mechanics* **835**, 393-405 (2018).
- 14 Wensink, H. H. *et al.* Meso-scale turbulence in living fluids. *Proceedings of the National Academy of Sciences* **109**, 14308-14313 (2012).
- 15 Dunkel, J. *et al.* Fluid dynamics of bacterial turbulence. *Physical Review Letters* **110**, 228102 (2013).
- 16 Shankar, S. & Marchetti, M. C. Hydrodynamics of active defects: From order to chaos to defect ordering. *Physical Review X* **9**, 041047 (2019).
- 17 Bratanov, V., Jenko, F. & Frey, E. New class of turbulence in active fluids. *Proceedings of the National Academy of Sciences* **112**, 15048-15053 (2015).
- 18 Toner, J., Tu, Y. & Ramaswamy, S. Hydrodynamics and phases of flocks. *Annals of Physics* **318**, 170-244 (2005).
- 19 Toner, J. & Tu, Y. Flocks, herds, and schools: A quantitative theory of flocking. *Physical Review E* **58**, 4828-4858 (1998).
- 20 Ramaswamy, S. The mechanics and statistics of active matter. *Annual Review of Condensed Matter Physics* **1**, 323-345 (2010).
- 21 Aditi Simha, R. & Ramaswamy, S. Hydrodynamic fluctuations and instabilities in ordered suspensions of self-propelled particles. *Physical Review Letters* **89**, 058101 (2002).
- 22 Thampi, S. P. & Yeomans, J. M. Active turbulence in active nematics. *The European Physical Journal Special Topics* **225**, 651-662 (2016).
- 23 Thampi, S. P., Golestanian, R. & Yeomans, J. M. Vorticity, defects and correlations in active turbulence. *Philosophical Transactions of the Royal Society A: Mathematical, Physical and Engineering Sciences* **372**, 20130366 (2014).
- 24 Giomi, L. Geometry and topology of turbulence in active nematics. *Physical Review X* **5**, 031003 (2015).

- 25 Urzay, J., Doostmohammadi, A. & Yeomans, J. M. Multi-scale statistics of turbulence motorized by active matter. *Journal of Fluid Mechanics* **822**, 762-773 (2017).
- 26 Cahn, J. W. & Hilliard, J. E. Free energy of a nonuniform system. I. Interfacial free energy. *The Journal of Chemical Physics* **28**, 258-267 (1958).
- 27 Anderson, D. M., McFadden, G. B. & Wheeler, A. A. Diffuse-interface methods in fluid mechanics. *Annual Review of Fluid Mechanics* **30**, 139-165 (1998).
- 28 Woodhouse, F. G. & Goldstein, R. E. Spontaneous circulation of confined active suspensions. *Physical Review Letters* **109**, 168105 (2012).
- 29 Doi, M. & Edwards, S. F. *The Theory of Polymer Dynamics*. (Clarendon Press, 2013).
- 30 Gao, T., Blackwell, R., Glaser, M. A., Betterton, M. D. & Shelley, M. J. Multiscale modeling and simulation of microtubule--motor-protein assemblies. *Physical Review E* **92**, 062709 (2015).
- 31 Ezhilan, B., Shelley, M. J. & Saintillan, D. Instabilities and nonlinear dynamics of concentrated active suspensions. *Physics of Fluids* **25**, 070607 (2013).
- 32 Jeffery, G. B. & Filon, L. N. G. The motion of ellipsoidal particles immersed in a viscous fluid. *Proceedings of the Royal Society of London. Series A, Containing Papers of a Mathematical and Physical Character* **102**, 161-179 (1922).
- 33 Gao, T., Betterton, M. D., Jhang, A.-S. & Shelley, M. J. Analytical structure, dynamics, and coarse graining of a kinetic model of an active fluid. *Physical Review Fluids* **2**, 093302 (2017).
- 34 Chaikin, P. M. & Lubensky, T. C. *Principles of Condensed Matter Physics*. Vol. 1 (Cambridge University Press, 2000).
- 35 Mittal, S. & Kumar, B. A stabilized finite element method for global analysis of convective instabilities in nonparallel flows. *Physics of Fluids* **19**, 088105 (2007).
- 36 TaoHe. An efficient selective cell-based smoothed finite element approach to fluid-structure interaction. *Physics of Fluids* **32**, 067102 (2020).
- 37 Holzbecher, E. Convection pattern formation in a domain with a horizontal interface. *Physics of Fluids* **31**, 056602 (2019).
- 38 Bendaraa, A., Charafi, M. M. & Hasnaoui, A. Numerical study of natural convection in a differentially heated square cavity filled with nanofluid in the presence of fins attached to walls in different locations. *Physics of Fluids* **31**, 052003 (2019).
- 39 Li, Q., Ito, K., Wu, Z., Lowry, C. S. & Loheide II, S. P. COMSOL Multiphysics: A novel approach to ground water modeling. *Groundwater* **47**, 480-487 (2009).
- 40 Rausch, M. H., Kretschmer, L., Will, S., Leipertz, A. & Fröba, A. P. Density, surface tension, and kinematic viscosity of hydrofluoroethers HFE-7000, HFE-7100, HFE-7200, HFE-7300, and HFE-7500. *Journal of Chemical & Engineering Data* **60**, 3759-3765 (2015).
- 41 Gittens, G. J. Variation of surface tension of water with temperature. *Journal of Colloid and Interface Science* **30**, 406-412 (1969).
- 42 Fan, Y., Wu, K.-T., Aghvami, A., Fraden, S. & Breuer, K. Effects of confinement on the dynamics and correlation scales in active fluids. arXiv:2103.06334 [cond-mat.soft] (2021).
- 43 Varghese, M., Baskaran, A., Hagan, M. F. & Baskaran, A. Confinement-induced self-pumping in 3D active fluids. *Physical Review Letters* **125**, 268003 (2020).
- 44 Chandragiri, S., Doostmohammadi, A., Yeomans, J. M. & Thampi, S. P. Flow states and transitions of an active nematic in a three-dimensional channel. *Physical Review Letters* **125**, 148002 (2020).
- 45 Chandrakar, P. *et al.* Confinement controls the bend instability of three-dimensional active liquid crystals. *Physical Review Letters* **125**, 257801 (2020).
- 46 Sanchez, T. *et al.* Combined noninvasive metabolic and spindle imaging as potential tools for embryo and oocyte assessment. *Human Reproduction* **34**, 2349-2361 (2019).
- 47 Lemma, L. M. *et al.* Multiscale Dynamics in Active Nematics. arXiv:2006.15184 [cond-mat.soft] (2020).
- 48 Lemma, L. M., Decamp, S. J., You, Z., Giomi, L. & Dogic, Z. Statistical properties of autonomous flows in 2D active nematics. *Soft Matter* **15**, 3264 (2019).

- 49 DeCamp, S. J., Redner, G. S., Baskaran, A., Hagan, M. F. & Dogic, Z. Orientational order of motile defects in active nematics. *Nature Materials* **14**, 1110-1115 (2015).
- 50 Opathalage, A. *et al.* Self-organized dynamics and the transition to turbulence of confined active nematics. *Proceedings of the National Academy of Sciences* **116**, 4788-4797 (2019).
- 51 Norton, M. M. *et al.* Insensitivity of active nematic liquid crystal dynamics to topological constraints. *Physical Review E* **97**, 012702 (2018).
- 52 Guillamat, P., Ignés-Mullol, J., Shankar, S., Marchetti, M. C. & Sagués, F. Probing the shear viscosity of an active nematic film. *Physical Review E* **94**, 060602 (2016).
- 53 Guillamat, P., Ignés-Mullol, J. & Sagués, F. Taming active turbulence with patterned soft interfaces. *Nature Communications* **8**, 564 (2017).
- 54 Guillamat, P., Hardoüin, J., Prat, B. M., Ignés-Mullol, J. & Sagués, F. Control of active turbulence through addressable soft interfaces. *Journal of Physics: Condensed Matter* **29**, 504003 (2017).
- 55 Putzig, E., Redner, G. S., Baskaran, A. & Baskaran, A. Instabilities, defects, and defect ordering in an overdamped active nematic. *Soft Matter* **12**, 3854-3859 (2016).
- 56 Doostmohammadi, A., Ignés-Mullol, J., Yeomans, J. M. & Sagués, F. Active nematics. *Nature Communications* **9**, 3246 (2018).
- 57 Thielicke, W. & Stamhuis, E. J. PIVlab—Towards user-friendly, affordable and accurate digital particle image velocimetry in MATLAB. *Journal of Open Research Software* **2**, e30 (2014).